Control of self-excited thermoacoustic oscillations using transient forcing, hysteresis and mode switching

Yu Guan[a], Wei He[a,c], Meenatchidevi Murugesan[a], Qiang Li[b], Peijin Liu[b], Larry K.B. Li[a,*]

[a] *Department of Mechanical and Aerospace Engineering, The Hong Kong University of Science and Technology, Clear Water Bay, Hong Kong*
[b] *Combustion, Internal Flow and Thermal-Structure Laboratory, Northwestern Polytechnical University, Xi'an, China*
[c] *School of Engineering, The University of Liverpool, L69 3GH, United Kingdom*

Abstract

In many combustion devices, strong self-excited flow oscillations can arise from feedback between unsteady heat release and acoustics, resulting in increased vibration and pollutant emissions. Open-loop acoustic forcing has been shown to be effective in weakening such thermoacoustic oscillations, but current implementations of this control strategy require the forcing to be continuously applied. In this proof-of-concept study, we experimentally demonstrate an alternative method of weakening thermoacoustic oscillations in a self-excited combustion system – a laminar premixed flame in a double open-ended tube. Unlike existing methods, the proposed method combines the use of transient forcing with hysteresis and mode switching, thus avoiding the need to continuously supply energy to the control system. Control is achieved by exploiting the fact that most combustors have a multitude of natural thermoacoustic modes, some of which are linearly unstable but some are nonlinearly unstable. By applying open-loop acoustic forcing at an off-resonance frequency and at an amplitude higher than that required for synchronization, we find that the combustor can switch to one of the nonlinearly unstable natural modes (f_2) and remain there, even after the forcing is removed. Dynamic mode decomposition of high-speed chemiluminescence videos shows that this mode switching occurs because the flame structure at f_2 is more robust than that at the original linearly unstable natural mode. The final unforced state has a thermoacoustic amplitude of just half that of the initial unforced state, even though the Rayleigh index of the former is higher than that of the latter. Although this 50% reduction in thermoacoustic amplitude is not as large as the 95% reduction achieved with asynchronous quenching, it is achieved without the use of continuous forcing. This is a distinct advantage over existing control strategies as it allows the complexity and power requirements of the control system to be reduced. With

*Corresponding author
Email address: larryli.ust.hk (Larry K.B. Li)

further development and testing, particularly on turbulent swirling combustors, the proposed control strategy could pave the way for a new class of open-loop control techniques based on transient forcing rather than continuous forcing.

Keywords: thermoacoustics, combustion instability, open-loop control, flame dynamics, gas turbines

1. Introduction

Thermoacoustic instability is a recurring problem in many combustion devices, such as industrial furnaces, rocket engines and gas turbines [1]. It is caused by resonant coupling between the acoustic modes of a combustor and the heat-release-rate (HRR) oscillations of the flame [2]. If this coupling is such that the acoustic pressure and HRR are sufficiently in phase with each other, the latter can transfer thermal energy to the former via the Rayleigh mechanism [3], resulting in self-excited flow oscillations at one or more of the natural acoustic frequencies of the combustor [4]. Such thermoacoustic oscillations, arising from flame–acoustic feedback, can lead to a variety of damaging effects, including flame blow-off and flashback, excessive vibration, and elevated pollutant emissions [1], reducing the efficiency, reliability and environmental performance of the combustion system [5]. Furthermore, recent environmental regulations have been calling for renewed reductions in the emissions of nitrogen oxides (NOx), prompting gas-turbine manufacturers to switch to lean-premixed combustion [6]. However, lean-premixed combustion is known to increase the propensity for thermoacoustic instability to occur [7]. Understanding the physical mechanisms responsible for this in practical combustion devices has been an ongoing challenge [4], not least because various driving mechanisms (e.g. coupling via equivalence-ratio oscillations [8], entropy waves [9] and vortical structures [10]) can coexist and interact with each other in non-trivial ways [1, 2]. Consequently, it would be useful to explore alternative strategies for weakening thermoacoustic oscillations in combustion systems.

1.1. Open-loop control of thermoacoustic oscillations

One such alternative is active control [2, 11]. This involves externally modulating one or more of the physical parameters of the system (e.g. the air or fuel flow rate [12–14], equivalence ratio [15, 16], or acoustic boundary conditions [17, 18]) in an effort to minimize the deviation between a target state and the actual operating state of the system [19]. The simplest form of active control is open-loop control, which requires just a single actuator (e.g. a loudspeaker or a fuel-modulation valve) and no sensors or feedback controllers, both of which can be unreliable under the harsh operating conditions of most combustors [2, 20].

1.1.1. Open-loop control as a forced synchronization process

Open-loop control is most intuitively studied in the nonlinear framework of forced synchronization [21]. In forced synchronization, external off-resonance forcing is applied to a self-excited system oscillating at a discrete natural frequency [22]. If the forcing amplitude is low, the system oscillates at both the natural frequency and the forcing frequency, leading to quasiperiodicity at these two incommensurate frequencies, as represented in phase space by a stable ergodic $\mathbb{T}^2$ torus attractor [22]. However, if the forcing amplitude is sufficiently high, the system locks into the forced mode, leaving no sign of the original natural mode [22]. The system is then said to have transitioned to a state known as *synchronization*, in which the dynamics are completely dictated by the forcing [21]. In recent years, several experimental and numerical studies have been carried out to exploit forced synchronization for open-loop control of hydrodynamically self-excited systems, such as low-density jets [23, 24], jet diffusion flames [25, 26], cross-flowing jets [27] and cylinder wakes [28]. Collectively, these studies show that when its amplitude and frequency are suitably chosen, open-loop forcing can be an effective means of controlling hydrodynamically self-excited oscillations in fluid systems. In the present study, one of the key objectives is to see how such forcing can be used to more effectively control thermoacoustically self-excited oscillations in combustion systems.

1.1.2. Previous studies on open-loop control of thermoacoustic oscillations

For combustion systems, one of the simplest forms of open-loop control is the application of periodic acoustic forcing. This type of forcing has been shown to be effective in weakening thermoacoustic oscillations in a variety of combustion systems, ranging from the simple Rijke tube (Reynolds numbers of $Re \sim 10^3$ with natural frequencies of $f_1 \sim 10^2$ Hz) [29–31] to turbulent premixed bluff-body combustors ($Re \sim 10^4$, $f_1 \sim 10^2$ Hz) [32, 33]. Open-loop acoustic forcing has even been shown to be effective in a model liquid-rocket combustor undergoing high-frequency thermoacoustic oscillations ($f_1 \sim 10^3$ Hz) [34]. In most of these studies [29–34], periodic acoustic forcing of different amplitudes and frequencies was applied to a self-excited combustor, with the aim of exploring the nonlinear dynamics leading up to synchronization. For example, on applying off-resonance forcing to a laminar premixed flame in a tube, Guan *et al.* [30] found (i) a transition from unforced periodicity to $\mathbb{T}^2$ quasiperiodicity via a Neimark–Sacker bifurcation; (ii) a transition from $\mathbb{T}^2$ quasiperiodicity to synchronization at a critical forcing amplitude, which increases with frequency detuning; (iii) a $\vee$-shaped Arnold tongue centered on the natural frequency; (iv) two distinct routes to synchronization, one via an inverse Neimark–Sacker bifurcation and one via a saddle-node bifurcation; and (v) that all of these dynamics could be qualitatively modelled with a forced Duffing–van der Pol oscillator. In a related example, Balusamy *et al.* [33] applied similar off-resonance forcing to a swirl-stabilized turbulent premixed combustor and found additional synchronization dynamics, such as frequency pulling and pushing as well as phase drifting, slipping, locking and trapping – the latter a partially synchronized state characterized by frequency locking without phase locking [24].

Perhaps most importantly, several researchers [29–34] – beginning with Bellows *et al.* [32] – have shown that near the onset of synchronization, the thermoacoustic amplitude can be substantially reduced (often to less than 50% of that of the initial unforced state) through a nonlinear process known as *asynchronous quenching*[1] [37]. Here asynchronous quenching refers to the reduction in thermoacoustic amplitude produced by the open-loop application of external periodic forcing at a frequency sufficiently far from the natural frequency for there to be no resonant amplification of the forcing [38]. Asynchronous quenching has been shown to coincide with an inverse Neimark–Sacker bifurcation to synchronization as well as a reduced Rayleigh index [30]. This shows that the open-loop application of periodic acoustic forcing can not only shift the natural frequency of a self-excited combustor to a target frequency (i.e. the forcing frequency) but it can also simultaneously reduce the thermoacoustic amplitude. Although these features are useful for mitigating thermoacoustic instability, they come with several trade-offs, one of which is the need for external forcing to be *continuously* applied. Should the forcing system malfunction during synchronization, the combustor would revert to its original unforced state, returning the thermoacoustic amplitude to its initial high value. Given this risk, it would be helpful to develop an alternative control strategy in which the proven benefits of open-loop forcing, such as a reduced thermoacoustic amplitude [29–34], can be achieved and maintained without the need for continuous forcing. The experimental demonstration of such a control strategy is the focus of this study.

1.2. Mode switching and hysteresis in thermoacoustic systems

In thermoacoustics, mode switching typically refers to a combustor switching from one natural mode to another, either as a function of time [39] or in response to variations in a control parameter [4]. Mode switching is often accompanied by hysteresis and is a characteristic feature of combustors operating in the nonlinear regime [40]. For example, Noiray *et al.* [41] found that a premixed multi-flame combustion system can switch hysteretically from one self-excited thermoacoustic mode to another as the length of the upstream acoustic plenum is varied. Hong *et al.* [42] found that a backward-facing step combustor can switch between three distinct natural modes as the equivalence ratio is varied. Zhao *et al.* [43] found that a swirl combustor can switch between the fundamental mode and its higher harmonics as the equivalence ratio is varied. Ahn *et al.* [44] found that a liquid-fuelled gas-turbine combustor can switch between a longitudinal mode and a Helmholtz mode as the combustor length is varied. Moeck *et al.* [45] found that a natural-gas-fuelled gas-turbine combustor can switch randomly in time between two stable limit-cycle modes as a result of turbulence-induced noise. However, to the best of our knowledge, mode switching due to the open-loop application of periodic acoustic forcing has not been reported before. Crucially, it has yet to be shown how mode switching can be integrated into an open-loop control strategy in such a way that thermoacoustic oscillations can be weakened without having to apply continuous forcing.

[1] This process is related to, but different from, the phenomenon of *amplitude death*, which has also been observed in self-excited thermoacoustic oscillators [35, 36] but requires mutual synchronization rather than forced synchronization.

1.3. Contributions of the present study

In this experimental study, we focus on two main research objectives:

(i) The first objective is to demonstrate, as proof of concept, an alternative method of weakening thermoacoustic oscillations in a self-excited combustion system. Unlike existing methods (see Sec. 1.1.2), the proposed method combines the use of transient forcing with hysteresis and mode switching, thus avoiding the need to continuously supply energy to the control system. To achieve this, we exploit the fact that most combustors have a multitude of natural thermoacoustic modes, some of which are linearly unstable but some are nonlinearly unstable[2] [1, 46, 47]. We hypothesize that if one of the nonlinearly unstable natural modes could be triggered with sufficiently strong forcing, the combustor might switch to that mode and lock onto it, even when the forcing is removed. If that new natural mode has a lower thermoacoustic amplitude than the original natural mode, then that could be a viable strategy for weakening thermoacoustic oscillations without the need for continuous forcing – thus allowing the complexity and power requirements of the control system to be reduced. This is the main novelty of our proposed control method.

(ii) The second objective is to investigate, from a more exploratory angle, the nonlinear dynamics beyond the onset of synchronization. As Sec. 1.1.2 has shown, although much research has already been conducted on open-loop control of combustion systems using acoustic forcing [29–34], most of that work has focused on the dynamics leading up to synchronization – not beyond it. A key question arises: What happens when the forcing amplitude increases above that required for synchronization? Does the combustor remain synchronized? Or does it switch to another self-excited state? If so, what are the dynamical properties of that new state? It is important to address these questions if one is to fully exploit open-loop forcing for control of thermoacoustic oscillations in combustion systems.

This paper is organized as follows. We describe the experimental setup and measurement diagnostics in Sec. 2, present the experimental results and discussion in Sec. 3, and conclude with the key findings and implications of this study in Sec. 4.

2. Experimental setup

Experiments are performed on a thermoacoustic system consisting of a ducted laminar premixed flame subjected to periodic acoustic forcing. Figure 1 shows

[2]Here the term 'nonlinearly unstable natural mode' is used to refer to a mode with two stable states: (i) a fixed point of zero amplitude and (ii) a limit cycle of finite amplitude [46]. The fixed point is stable to small-amplitude perturbations but is unstable to large-amplitude perturbations [1]. Therefore, when the mode is at the stable fixed point, a sufficiently large perturbation (e.g. from external forcing) can push it into the basin of attraction of the stable limit cycle – a process sometimes referred to as 'triggering' in thermoacoustics [1, 46, 47].

the setup, which is similar to that of our previous study on controlling thermoacoustic oscillations using continuous forcing [30] and is modelled after the numerical configuration of Kashinath *et al.* [29]. The system has four main components: a double open-ended quartz tube combustor (inner diameter, ID: 44 mm; length: $L = 860$ mm), a stainless steel burner (ID: $D = 16.8$ mm; length: 800 mm), an acoustic decoupler (ID: 180 mm; length: 200 mm) and a loudspeaker for acoustic forcing. At the burner exit, a copper extension tip (ID: 12 mm; length: 30 mm) containing a fine-mesh screen is installed to enhance flame stabilization. A rotameter ($\pm 2.5\%$) is used to control the flow rate of fuel (liquefied petroleum gas: 70% butane and 30% propane), while a mass flow controller (Alicat MCR series: $\pm 0.2\%$ FS) is used to control the flow rate of air. An upstream mixing chamber is used to ensure that the fuel and air are thoroughly mixed prior to reaching the burner inlet.

Although this thermoacoustic system can exhibit a wide range of nonlinear states (including quasiperiodicity and chaos), we focus on the simplest possible self-excited state: a periodic limit cycle. In our combustor, this state can be found at an equivalence ratio of 0.62 ($\pm 3.2\%$); a bulk reactant velocity of $\bar{u} = 1.6$ m/s ($\pm 0.2\%$); a Reynolds number of $Re \equiv \rho \bar{u} D/\mu = 1300$, where ρ and μ are the density and dynamic viscosity of the reactants; and a flame position of $x_f \equiv x/L = 0.58 \pm 0.002$, where x is the distance between the burner lip and the bottom of the combustor (see Fig. 1). At this operating condition, the natural frequency of the limit-cycle oscillations is $f_1 = 254 \pm 1.5$ Hz, and the modal structure is a 1-st harmonic standing wave with a pressure anti-node near the midpoint of the double open-ended tube combustor.

The thermoacoustic system is acoustically forced at different amplitudes and frequencies around its natural frequency ($0.9 \leqslant f_f/f_1 \leqslant 1.1$) in order to explore its synchronization dynamics under various regimes of open-loop control. A digital function generator (Keysight 33512B) is used to generate a sinusoidal forcing signal, which is amplified by a power amplifier (Alesis RA150) before being fed into a loudspeaker (FaitalPRO 6FE100) mounted in the acoustic decoupler (see Fig. 1). The forcing amplitude, which is measured with a constant-temperature hot wire (DANTEC MiniCTA and a 55P16 probe), is defined as $\epsilon_f \equiv u'/\bar{u}$, where u' is the velocity perturbation amplitude at the burner outlet and $\bar{u}$ is the time-averaged velocity of the bulk reactants issuing from the burner.

Simultaneous measurements of the acoustic pressure and HRR are made to quantify the synchronization dynamics of the system via the Rayleigh index. The acoustic pressure is measured with two probe microphones (GRAS 40SA: sensitivity of 3 mV/Pa, $\pm 2.5 \times 10^{-5}$ Pa) mounted 43 mm (PM-1) and 387 mm (PM-2) from the bottom of the combustor. These microphones are calibrated against a certified sound source (Brüel & Kjær Type 4231). The analog output from these microphones is digitized at 65536 Hz for 6 s on a 16-bit data acquisition system. The HRR is measured in two different ways: (i) via the CH* chemiluminescence signal, as detected with a photomultiplier tube (Thorlabs PMM01; $\pm 1.5\%$) viewing through a bandpass filter centered on 430 nm, and (ii) via broadband chemiluminescence, as recorded with a high-speed camera (Photron FASTCAM SA-Z) operating at 4000 frames/s, with an image resolution of 512×512 pixels and a bit depth of 12. This frame rate is more than 15 times the natural frequency of the self-excited thermoacoustic oscillations ($f_1 = 254 \pm 1.5$ Hz) and is thus high enough for the imaging to be considered time resolved. These high-speed chemiluminescence videos, serving as proxies for the spatial distribution of HRR [48], are analyzed with dynamic mode decomposition (DMD) in order to extract the dominant HRR structures of the flame at the frequencies of interest, as will be discussed in Sec. 3.2.

3. Results and discussion

3.1. Forced synchronization of the thermoacoustic system

In this section, we examine the forced synchronization of the thermoacoustic system, focusing on mode switching, hysteresis, and the dynamical states appearing before and after the onset of synchronization. The system is forced over a wide range of amplitudes ($0 \leqslant \epsilon_f \leqslant 30\%$) and frequencies ($0.9 \leqslant f_f/f_1 \leqslant 1.1$) but, for the purposes of demonstration and conciseness, only results from the most representative forcing conditions are shown. Figure 2 shows the (a) time trace, (b) power spectral density (PSD) and (c) Poincaré map of the acoustic pressure (p' from PM-2) in the combustor at $f_f/f_1 = 1.08$, with the forcing amplitude ($\epsilon_f \equiv u'/\bar{u}$, expressed in %) starting from zero (an unforced state), increasing to a value above that required for synchronization, and then decreasing back to zero (another unforced state).

3.1.1. Natural dynamics: a periodic limit cycle

When unforced (Fig. 2, bottom row in burgundy: $\epsilon_f = 0.0\%$), the combustor is thermoacoustically self-excited, oscillating in a limit cycle at a natural frequency of f_1. This is evidenced by a regular waveform in the time trace and by a clear peak at $f/f_1 = 1$ in the PSD. There are also weaker peaks at the higher harmonics (not shown), indicating that the acoustic pressure is not oscillating perfectly sinusoidally in time. In the Poincaré map, there are two isolated points, indicating that the phase trajectory is a closed loop – a characteristic feature of a periodic limit cycle [49]. This unforced state is classified as a period-1 (P1) limit cycle because its phase trajectory loops around itself once every cycle. This state is labelled as $\mathrm{P1}_1$, where the subscript 1 indicates that the combustor dynamics are dominated by the natural mode at f_1.

3.1.2. Approaching synchronization: two-frequency quasiperiodicity

When the forcing amplitude is low (Fig. 2, pink: $\epsilon_f = 2.2\%$), the combustor responds at both the natural frequency (f_1) and the forcing frequency (f_f), as well as at their linear combinations, resulting in sidebands in the PSD and amplitude modulations in the time trace at a beating frequency of $|f_f - f_1|$. In the Poincaré map, two closed rings emerge, indicating that the combustor has transitioned from an unforced periodic state to a two-frequency quasiperiodic state via a Neimark–Sacker bifurcation [22]. These are the classical features of a forced self-excited oscillator before the onset of synchronization [21]. This state is classified as a two-frequency quasiperiodic state because its phase trajectory spirals around the surface of a stable ergodic torus attractor with two incommensurate modes [21]: the natural mode (f_1) and the forced mode (f_f). This state is therefore labelled as $\mathrm{T}^2_{1,f}$.

3.1.3. Onset of synchronization: periodicity and asynchronous quenching

When forced above a critical amplitude ($\epsilon_f = 3.8\%$; for example, Fig. 2, green: $\epsilon_f = 7.1\%$), the combustor synchronizes with the forcing. This is evidenced by the PSD becoming dominated by a single peak at f_f, with no sign of the original natural mode at f_1. Moreover, the two rings in the Poincaré map collapse into two discrete points, indicating a transition from a two-frequency quasiperiodic state to a synchronized periodic state [22]. In phase space, this transition coincides with the collapse of the $\mathrm{T}^2_{1,f}$ torus attractor into a stable periodic orbit at f_f via an inverse Neimark–Sacker bifurcation [30]. The time trace no longer exhibits modulations. Instead, its oscillation amplitude becomes significantly smaller than that of the initial unforced state ($\mathrm{P1}_1$: $\epsilon_f = 0.0\%$). Similar reductions in the thermoacoustic amplitude have been reported before in experiments [30] and numerical simulations [29] on forced self-excited ducted flames. Such reductions can be attributed to *asynchronous quenching* [37], which will be examined further in Sec. 3.1.6. This periodic state is classified as a synchronized P1 state because its phase trajectory loops repeatedly around a closed orbit at f_f. This state is therefore labelled as $\mathrm{P1}_f$.

For a fixed value of f_f/f_1, the maximum amplitude reduction typically occurs at the onset of synchronization, i.e. just beyond the boundary between $\mathrm{T}^2_{1,f}$ and $\mathrm{P1}_f$. Figure 3(a) shows the thermoacoustic amplitude at the onset of synchronization as a function of f_f/f_1. Here the thermoacoustic amplitude is normalized by its reference value at the initial unforced state ($\mathrm{P1}_1$): $\widetilde{p}'_{sync} \equiv p'_{\mathrm{RMS},sync}/p'_{\mathrm{RMS,P1}_1}$. It can be seen that $\widetilde{p}'_{sync}$ exceeds 1 at frequencies slightly below $f_f/f_1 = 1$. This is consistent with the fact that asynchronous quenching cannot occur if f_f/f_1 is not sufficiently far from 1, as demonstrated by experiments [30] and G-equation simulations [29] of forced ducted premixed flames, and by theoretical analyses of forced self-excited oscillators [50]. Nevertheless, as f_f/f_1 deviates further from 1, $\widetilde{p}'_{sync}$ drops below 1, which is consistent with an inverse Neimark–Sacker bifurcation to synchronization with asynchronous quenching [30]. The minimum forcing amplitude required to produce synchronization increases as f_f/f_1 deviates from 1, as shown in Fig. 3(b). This is a classical feature of periodically forced self-excited oscillators [21, 22].

It is clear that asynchronous quenching is a promising strategy for weakening thermoacoustic oscillations. After all, as previous studies [29–34] and our results show, the thermoacoustic amplitude can be reduced significantly at the onset of synchronization (by up to 95% in Fig. 3a).[3] In our setup, the average electrical power required by the loudspeaker to achieve asynchronous quenching when

[3]Note that this 95% reduction differs from the 90% reduction quoted in our earlier study [30] because the present study uses a smaller step-size for ϵ_f: 0.4% here vs. 0.8% in Ref. [30].

$0.9 \leqslant f_f/f_1 \leqslant 1.1$ is 8×10^{-2} W, which is less than 0.02% of the thermal power of the flame (430 W). Nevertheless, as mentioned earlier, this control strategy is not without its trade-offs, one of which is the need for external forcing to be continuously applied (Sec. 1.1.2). A key objective of the present study is to explore how the thermoacoustic amplitude can be reduced without the use of continuous forcing (Sec. 1.3). Thus, we shall proceed to increase ϵ_f further, to values above that required for synchronization, so as to excite one of the nonlinearly unstable natural modes and to ultimately induce mode switching.

3.1.4. Beyond synchronization: three-frequency quasiperiodicity

At sufficiently high forcing amplitudes (Fig. 2, purple: $8.7 \leqslant \epsilon_f \leqslant 12.7\%$), the original natural mode reemerges, as can be seen in the PSD by a sharp peak at f_1. This is important because it shows that acoustically forcing a self-excited thermoacoustic system beyond the onset of synchronization can cause that system to transition out of synchronization.

Besides the original natural mode (f_1) and the forced mode (f_f), a second natural mode emerges at f_2, which is not a rational multiple of f_1 or f_f. This new natural mode is linearly stable but nonlinearly unstable, because it becomes excited only after the forcing amplitude has reached a critically high value ($\epsilon_f \geqslant 8.7\%$ for $f_f/f_1 = 1.08$). This critically high value of the forcing amplitude increases as f_f/f_1 deviates from 1 – similar to the behavior of the synchronization boundary (see Fig. 3*b*). The excitation of this new mode is consistent with the observation that most combustors have a multitude of natural thermoacoustic modes, some of which are linearly unstable but some are nonlinearly unstable [1, 46, 47]. This opens up the possibility of mode switching, which will be explored in the next subsection. In phase space, this new mode gives rise to another stable ergodic torus attractor, but with three incommensurate frequencies: f_1, f_f and f_2. In the Poincaré map, the trajectory intercepts are stretched by the third frequency (f_2), resulting in a folded structure featuring two hollow intersecting rings, whose boundaries are more convoluted than those of the $\mathrm{T}^2_{1,f}$ attractor found at $\epsilon_f = 2.2\%$. The PSD has a large number of sharp peaks at linear combinations of the three incommensurate frequencies (f_1, f_2, f_f), while the amplitude of the time trace is modulated irregularly. The combustor remains at this quasiperiodic state until ϵ_f becomes high enough to blow out the flame. This state is classified as a three-frequency quasiperiodic state because its phase trajectory spirals around the surface of a torus attractor with three incommensurate modes: the original natural mode (f_1), the nonlinearly unstable natural mode (f_2), and the forced mode (f_f). This state is therefore labelled as $\mathrm{T}^3_{1,2,f}$.

3.1.5. Returning to an unforced state: mode switching and hysteresis

In previous studies on open-loop control of thermoacoustic systems (Sec 1.1.2), synchronization was reached exclusively by increasing ϵ_f, with no retracement through subsequent decreases in ϵ_f. Thus, the possibility of hysteresis could not be explored. Another feature that could not be explored is the control strategy proposed in Sec. 1.3, which involves (i) forcing a self-excited combustor such that it switches to another, less damaging, natural mode, (ii) removing the forcing altogether, and then (iii) allowing the system to persist on that new natural mode, thereby reducing the thermoacoustic amplitude without having to use continuous forcing. In this subsection, we not only increase ϵ_f above that required for synchronization, but then decrease it back to zero (unforced state) so as to explore the reversibility of the synchronization path and the viability of using mode switching to weaken thermoacoustic oscillations.

When the forcing amplitude is reduced from the value required for $\mathrm{T}^3_{1,2,f}$ (Fig. 2: $\epsilon_f = 8.7 \rightarrow 2.2\%$), the combustor transitions to a two-frequency quasiperiodic state without passing through an intermediate synchronized state. This bypassing of a synchronized state is in stark contrast to the $\mathrm{P1}_f$ state observed when ϵ_f increases towards synchronization (Fig. 2: $\epsilon_f = 2.2 \rightarrow 7.1 \rightarrow 8.7\%$). This new two-frequency quasiperiodic state ($\mathrm{T}^2_{2,f}$) is dominated by f_2 and f_f, with no sign of the original natural mode at f_1. The two-frequency nature of this state is corroborated by the emergence of two closed rings in the Poincaré map. Crucially, this two-frequency quasiperiodic state ($\mathrm{T}^2_{2,f}$) differs from the one ($\mathrm{T}^2_{1,f}$) found when ϵ_f increases from 0.0 to 2.2%. That earlier torus attractor was formed from the original (linearly unstable) natural mode (f_1) and the forced mode (f_f), whereas the present one is formed from the new (nonlinearly unstable) natural mode (f_2) and the forced mode (f_f). This shows that the combustor can be attracted to different dynamical states depending on the specific synchronization route taken, with $\mathrm{T}^2_{1,f}$ appearing when ϵ_f increases towards synchronization and with $\mathrm{T}^2_{2,f}$ appearing when ϵ_f increases beyond synchronization and then decreases. To the best of our knowledge, this is the first definitive evidence of mode switching and hysteresis occurring in a thermoacoustically self-excited combustor undergoing forced synchronization.

When the forcing amplitude is reduced to zero (Fig. 2, top row in navy: $\epsilon_f = 0.0\%$), the combustor returns to a periodic state. However, unlike the initial periodic state found before the application of forcing (Fig. 2, bottom row in burgundy: $\epsilon_f = 0.0\%$), which was dominated by f_1, here the final periodic state is dominated by f_2, as evidenced in the PSD by a sharp peak at $f_2/f_1 = 0.74$. This constitutes further evidence of hysteresis and mode switching. The spectral peak at $f_2/f_1 = 0.74$ is accompanied by weaker peaks at its higher harmonics ($2f_2$ is shown), indicating that the oscillations are not perfectly sinusoidal in time. The Poincaré map shows two discrete points, confirming that the phase trajectory is indeed a closed-loop orbit, a distinguishing feature of a periodic limit cycle [49]. This state is labelled as $\mathrm{P1}_2$ because the combustor dynamics are dominated by the nonlinearly unstable natural mode at f_2. Such mode switching indicates that the combustor has multiple stable states, some of which, like $\mathrm{P1}_2$, can only be reached via the application and subsequent removal of strong forcing. Crucially, the time trace, PSD and Poincaré map all show that this final unforced state ($\mathrm{P1}_2$) has a lower thermoacoustic amplitude than the initial unforced state ($\mathrm{P1}_1$), demonstrating that it is indeed possible to weaken thermoacoustic oscillations using transient forcing, hysteresis and mode switching. This control strategy will be examined further in the next subsection.

3.1.6. *Controlling self-excited thermoacoustic oscillations using transient forcing, hysteresis and mode switching*

To investigate the reduction in thermoacoustic amplitude observed between states P1_2 and P1_1, we show in Fig. 4 four system indicators, all of which are normalized by their respective values at the initial unforced state (P1_1) and are plotted against ϵ_f. These indicators are (a) the root mean square (RMS) of p' from PM-2: $\widetilde{p}' \equiv p'_{\mathrm{RMS}}/p'_{\mathrm{RMS,P1_1}}$; ($b$) the PSD of p'; (c) the RMS of the HRR fluctuation q' measured by PMT: $\widetilde{q}' \equiv q'_{\mathrm{RMS}}/q'_{\mathrm{RMS,P1_1}}$; and ($d$) the Rayleigh index: $\widetilde{\mathrm{RI}} \equiv \mathrm{RI}/\mathrm{RI}_{\mathrm{P1_1}}$ where $\mathrm{RI} \equiv 1/T \int_0^T p'(t) q'(t)\, dt$.

Along the forward path, as ϵ_f increases from zero (Fig. 4a), $\widetilde{p}'$ by definition starts from one at P1_1, decreases during $\mathrm{T}^2_{1,f}$, and then reaches a minimum of around 0.05 at the onset of synchronization P1_f. This reduction in $\widetilde{p}'$ is due to asynchronous quenching (see Sec. 3.1.3). As ϵ_f increases further, $\widetilde{p}'$ bounces off its minimum and increases throughout the rest of P1_f as well as into $\mathrm{T}^3_{1,2,f}$.

Along the return path, as ϵ_f decreases from its maximum, $\widetilde{p}'$ in $\mathrm{T}^3_{1,2,f}$ initially follows the same path down as it did on the way up. However, it eventually diverges to a hysteretic path along which a $\mathrm{T}^3_{1,2,f} \to \mathrm{T}^2_{2,f}$ transition occurs without an intermediate synchronized state. As ϵ_f approaches zero, $\widetilde{p}'$ approaches 0.48 at the final unforced state (P1_2), indicating that the thermoacoustic amplitude is nearly half that of the initial unforced state (P1_1). Although this reduction in $\widetilde{p}'$ is not nearly as large as the 95% reduction observed at the onset of synchronization (P1_f), it is achieved with a combination of transient forcing, hysteresis and mode switching – rather than with continuous forcing. As mentioned earlier, this is a unique feature of the proposed control strategy.

This sequence of state transitions (P$1_1 \to \mathrm{T}^2_{1,f} \to \mathrm{P}1_f \to \mathrm{T}^3_{1,2,f} \to \mathrm{T}^2_{2,f} \to$ P1_2) can also be seen in the PSD. As Fig. 4(b) shows, the initial unforced state (P1_1), which is at the start point on the path of increasing ϵ_f (bottom frame), has a natural frequency (f_1) different from that (f_2) of the final unforced state (P1_2), which is at the end point on the path of decreasing ϵ_f (top frame).

Given the sizable reduction in thermoacoustic amplitude observed between states P1_1 and P1_2, it is reasonable to expect $\widetilde{q}'$ to follow the same trend as $\widetilde{p}'$. However, as Fig. 4(c) shows, this is not the case here. Although there are many similarities between $\widetilde{q}'$ and $\widetilde{p}'$, including identical regions of hysteretic and non-hysteretic behavior, there are also some notable differences. Key among them is that $\widetilde{q}'$ for P1_2 is higher – by a factor of around four – than that for P1_1, despite P1_2 having a thermoacoustic amplitude ($\widetilde{p}'$) only half that of P1_1 (Fig. 4a). This observation is unexpected because a lower thermoacoustic amplitude is typically assumed to be associated with a lower HRR amplitude and, hence, a weaker thermoacoustic driving term. To explore the cause of the reduced $\widetilde{p}'$, we turn to the Rayleigh index, $\mathrm{RI} \equiv 1/T \int_0^T p'(t) q'(t)\, dt$ [1]. This is a quantitative measure of the direction and magnitude of the energy transfer between the flame and the acoustic field of the combustor. It accounts not just for the amplitude variations in q' and p' but also for their phase relationship [4].

Figure 4(d) shows that the Rayleigh index behaves qualitatively similarly to $\widetilde{q}'$ (Fig. 4c) in the sense that both quantities show hysteretic and non-hysteretic regions in the response curve. The Rayleigh index drops to a minimum near the onset of synchronization, which explains why the thermoacoustic amplitude also drops to a minimum there. However, the Rayleigh index for $\mathrm{P1}_2$ is higher than that for $\mathrm{P1}_1$, much like how $\widetilde{q}'$ for $\mathrm{P1}_2$ is higher than that for $\mathrm{P1}_1$. This shows that the phase lag between q' and p' has not changed sufficiently to overcome the dominance of the amplitude correlation between q' and p'. Nevertheless, the fact that the Rayleigh index varies between states $\mathrm{P1}_1$ and $\mathrm{P1}_2$ is further evidence that the coupling between the flame and its surrounding acoustic field has been irreversibly altered by the transient forcing and mode switching.

Although unexpected, the notion that $\widetilde{p}'$ does not necessarily have to follow the same trend as $\widetilde{\mathrm{RI}}$ or $\widetilde{q}'$ has been hinted at before. In experiments on a backward-facing step combustor, Hong *et al.* [42] varied the equivalence ratio and found that both the sound pressure level (Fig. 2 in [42]) and the HRR amplitude (Fig. 4 in [42]) can remain constant even when the phase difference between p' and q' increases from $0°$ to $45°$. This increase in the phase difference implies a decrease in the Rayleigh index (although it remains positive) and, hence, a decrease in the energy transferred from the flame to the acoustic field – even though the sound pressure level remains constant.

The combustor dynamics seen in Fig. 4 are not limited to just one value of f_f, but can be seen across a wide range of f_f around f_1 ($0.9 \leqslant f_f/f_1 \leqslant 1.1$), so long as synchronization occurs via an inverse Neimark–Sacker bifurcation [22, 30]. To illustrate this, we show in Fig. 5 the same four system indicators as in Fig. 4 but for $f_f/f_1 \approx 0.90$ instead of $f_f/f_1 \approx 1.08$. Qualitatively, the combustor can be seen to exhibit the same dynamics regardless of the exact value of f_f/f_1. These dynamics include (i) the existence of global minima in $\widetilde{p}'$ and $\widetilde{\mathrm{RI}}$ near the onset of synchronization, (ii) the coexistence of hysteretic and non-hysteretic regimes as ϵ_f varies, (iii) a reduction in $\widetilde{p}'$ between the final ($\mathrm{P1}_2$) and initial ($\mathrm{P1}_1$) unforced states, and (iv) an increase in $\widetilde{\mathrm{RI}}$ between states $\mathrm{P1}_2$ and $\mathrm{P1}_1$. The fact that such a detailed level of dynamical similarity is observed is not surprising given that many of the defining features of forced synchronization are known to be universal [21, 22].

Further quantitative analysis shows that the percentage reduction in $\widetilde{p}'$ achieved at the end of the backward path ($\mathrm{P1}_2$) does not depend on whether synchronization occurs via an inverse Neimark–Sacker bifurcation (f_f/f_1 far from 1) or a saddle-node bifurcation (f_f/f_1 close to 1). So long as the nonlinearly unstable natural mode at f_2 is excited, the system always returns to the same final unforced state ($\mathrm{P1}_2$) when the forcing is removed.

It should be noted that the large reduction in $\widetilde{p}'$ observed between states $\mathrm{P1}_2$ and $\mathrm{P1}_1$ (Figs. 4 and 5) occurs only if ϵ_f is increased to such a magnitude that it excites the nonlinearly unstable natural mode (f_2) and, in turn, the three-frequency quasiperiodic state ($\mathrm{T}^3_{1,2,f}$). This is because only after f_2 has been excited can the combustor switch to this new natural mode on removal of the forcing. By contrast, mode switching cannot occur if ϵ_f simply increases to a value just sufficient for synchronization ($\mathrm{P1}_f$) and then decreases to zero. To illustrate this, we show in Fig. 6 the same four indicators as in Figs. 4 and 5 but with ϵ_f increasing only up to the synchronized regime (not beyond it) and then decreasing back to zero. The absence of mode switching is evidenced by the dominance of f_1 in the PSD along both the forward path (Fig. 6*b*: bottom frame) and the backward path (Fig. 6*b*: top frame). Although $\widetilde{p}'$ is still significantly reduced by asynchronous quenching at the onset of synchronization (to around 5% of the initial unforced value), it returns to roughly the same initial value when ϵ_f decreases back to zero. This highlights the need to excite the nonlinearly unstable natural mode (f_2) if one is to reduce the thermoacoustic amplitude by transient forcing and mode switching.

In summary, this section has shown that it is readily possible to reduce the thermoacoustic amplitude of a self-excited combustor without the use of continuous forcing. By carefully applying transient forcing and exploiting the inherent hysteretic and mode-switching dynamics of the combustor, we can achieve a 50% reduction in $\widetilde{p}'$ between the final ($P1_2$) and initial ($P1_1$) unforced states. Although this is not as large as the 95% reduction achieved with asynchronous quenching at the onset of synchronization, the proposed control strategy has the unique advantage that it does not require external forcing to be continuously applied. This enables the complexity and power requirements of the control system to be reduced.

3.2. Dynamic mode decomposition

In thermoacoustics, it is well established that the flame dynamics play a key role in governing the transfer of thermal energy to the acoustic field (Sec. 1). To examine the flame dynamics during forced synchronization, it is helpful to decompose the HRR oscillations into frequency-specific modes, enabling the HRR structures at f_1 or f_2 to be isolated from those at f_f – or at any other frequency of interest. A proven way to do this is with dynamic mode decomposition (DMD) [51]. This is a modal decomposition technique relying on the reconstruction of a low-dimensional inter-snapshot map from time-resolved input data [52, 53]. The resultant dynamic modes are mutually orthogonal in time, which means that each mode oscillates at a single temporal frequency [51]. For our flame analysis, DMD is preferred over other decomposition techniques (such as proper orthogonal decomposition [54, 55]) because it enables the HRR structures associated with any one particular temporal frequency to be identified. Moreover, DMD enables the most persistent HRR structures to be identified over the observation interval, independent of their energy content [52]. DMD has previously been used to extract dynamical information from a variety of thermofluid systems, ranging from the Rijke tube [56] to turbulent swirling premixed flames [57–59] to model gas-turbine/rocket combustors [60].

In this study, to gain further insight into the mode-switching dynamics of the combustor (Sec. 3.1.6), we use DMD to examine the HRR structures of the ducted flame for the three broad classes of synchronization states identified in Figs. 2 and 4: periodic states ($P1_1$, $P1_2$, $P1_f$), two-frequency quasiperiodic states ($T^2_{1,f}$, $T^2_{2,f}$), and a three-frequency quasiperiodic state ($T^3_{1,2,f}$).

The DMD procedure adopted in this study follows Refs. [51, 52]. First, a sequence of 800 flame snapshots is extracted from each time-resolved chemiluminescence video (see Sec. 2). These snapshots, representing around 50 natural oscillation cycles at $f_1 = 254$ Hz, are transformed into two matrices, X_1 and X_2, as per Refs. [51, 52]. The singular value decomposition of X_1 is then performed as $X_1 = U\Sigma V^H$, where U and V are unitary matrices and Σ is a diagonal matrix containing the singular values of X_1. Next the modal structures are extracted from $\tilde{S} = U^H AU = U^H X_2 V\Sigma^{-1}$, and the dynamic modes are expressed as $\phi_i = U\mathbf{y_i}$, where $\mathbf{y_i}$ is the ith eigenvector of $\tilde{S}$, i.e. $\tilde{S}\mathbf{y_i} = \mu_i \mathbf{y_i}$. Finally, the frequencies ($f = \mathrm{Im}\,(\lambda_i/2\pi)$) and growth rates ($\sigma = \mathrm{Re}\,(\lambda_i)$) of the dynamic modes are found from the spectrum $\lambda_i = \frac{1}{\Delta t}\log(\mu_i)$, where Δt is the inverse of the sampling frequency and μ_i contains the eigenvalues.

3.2.1. Periodic states: P1_1, P1_2 *and* P1_f

Figure 7 shows the normalized amplitude ($\tilde{A}$) and growth rate (σ) of the DMD modes as a function of the normalized frequency ($\tilde{f} \equiv f/f_1$) for three different periodic states: P1_1, P1_2 and P1_f. For each state, the mode amplitude is normalized by the mode amplitude at 0 Hz, which is the highest in the spectrum. In the spectra shown in Figs. 7(a–c), the two most dominant modes are highlighted with colored markers. Because all three states are periodic, the two most dominant modes are the fundamental and the second harmonic, with the former at a higher amplitude than the latter, which is consistent with the trends observed in the PSD (Fig. 2b). For each of the three periodic states, the two most dominant modes have a growth rate of around zero (Fig. 7d–f), as would be expected for saturated oscillations at a limit cycle.

Figures 7(g–i) show the spatial distribution of the DMD modes at their respective dominant frequencies: (g) $\tilde{f} = 1.00$ for f_1, (h) $\tilde{f} = 0.74$ for f_2, and (i) $\tilde{f} = 1.08$ for f_f. There are many similarities but also some notable differences among these periodic modes. For all three modes, convective wavepackets, which are a typical feature of periodic flows [52], can be seen along the edges of the flame body. These wavepackets are symmetric with respect to the flame centerline, with each wavepacket representing one full wavelength of the modulation. The wavepackets on the inside of the flame front are consistently out of phase with those on the outside. For P1_1 and P1_f, the dominant frequencies (f_1, f_f) are very close to each other, resulting in these two states having a similar set of wavepackets. For P1_2, however, the nonlinearly unstable natural mode is excited, producing longer wavepackets because the dominant frequency (f_2) is lower than f_1 and f_f. The wavepackets for P1_2 are also wider than those for P1_1 and P1_f. Furthermore, they taper down in width from the flame base to the flame tip, whereas the opposite trend is observed for P1_1 and P1_f. This tapering towards the flame tip for P1_2 can be attributed to this state having a flame with a smaller radius of curvature and a smaller average height (see the insets in Fig. 7g–i) than those of P1_1 and P1_f. This concurs with our high-speed chemiluminescence videos, which show that shorter curvier flames, like that of P1_2, oscillate more strongly at the base than they do at the tip.

To illustrate this, we compare in Fig. 8 the instantaneous flame fronts of the two unforced periodic states: P1_1 and P1_2. Here the flame fronts are extracted from the chemiluminescence images by applying an inverse Abel transform and then tracking the locus of maximum pixel intensity. For both $\mathrm{P1}_1$ (Fig. 8*a*) and $\mathrm{P1}_2$ (Fig. 8*b*), clear evidence of cusp formation and pinch-off can be observed, consistent with previous studies on periodically oscillating conical premixed flames [61]. From Fig. 7, it is known that the $\mathrm{P1}_1$ flame oscillates at a higher frequency ($\tilde{f} = 1$) than the $\mathrm{P1}_2$ flame ($\tilde{f} = 0.74$), which explains why the former has shorter roll-up wrinkles than the latter. The flame front is wrinkled by a travelling wave propagating from the flame base to the flame tip [62]. Overlaying the two flames on top of each other (Fig. 8*c*), we find that the $\mathrm{P1}_2$ flame (shown in blue) oscillates with a larger amplitude than the $\mathrm{P1}_1$ flame (shown in red). This concurs with Fig. 4(*c*) in that $\widetilde{q}'$ is higher for $\mathrm{P1}_2$ than it is for $\mathrm{P1}_1$. Furthermore, we also find that the $\mathrm{P1}_2$ flame oscillates more strongly at its base than at its tip ($h_1/h_2 = 0.85$), whereas the opposite trend is observed in the $\mathrm{P1}_1$ flame ($d_1/d_2 = 1.55$). The $\mathrm{P1}_2$ flame front also has a smaller radius of curvature than the $\mathrm{P1}_1$ flame front. Taken together, these observations provide further evidence that shorter curvier flames, like that of $\mathrm{P1}_2$, oscillate more strongly at the base than they do at the tip.

Figures 7(*j*–*l*) show the spatial distribution of the DMD modes at their respective second harmonics: (*j*) $\tilde{f} = 2.00$ for $2f_1$, (*k*) $\tilde{f} = 1.48$ for $2f_2$, and (*l*) $\tilde{f} = 2.16$ for $2f_f$. The wavepackets in these modes are generally shorter than those at the dominant frequencies (Fig. 7*g*–*i*) because the second harmonics are higher in frequency. Most of the modal features identified at the dominant frequencies (Fig. 7*g*–*i*) are also present in the second harmonics (Fig. 7*j*–*l*).

In summary, this section has shown that while the DMD modes for all three periodic states exhibit a similar convective structure, the scale of the individual wavepackets depends on the dominant frequency of the flame dynamics. Crucially, the flame in the final unforced state ($\mathrm{P1}_2$) is found to oscillate more strongly than that in the initial unforced state ($\mathrm{P1}_1$), which is consistent with the higher values of $\widetilde{q}'$ and $\widetilde{\mathrm{RI}}$ observed for $\mathrm{P1}_2$ (see Sec. 3.1.6).

3.2.2. Two-frequency quasiperiodic states: $\mathrm{T}^2_{1,f}$ *and* $\mathrm{T}^2_{2,f}$

Figure 9 is analogous to Fig. 7 but for the two different two-frequency quasiperiodic states identified in Figs. 2 and 4: $\mathrm{T}^2_{1,f}$ and $\mathrm{T}^2_{2,f}$. For both states, the two most dominant modes are the natural mode (f_1 or f_2) and the forced mode (f_f), as shown in the DMD spectra of Figs. 9(*a*–*b*, *g*–*h*). The dominance of these two incommensurate modes is consistent with the pressure spectra of Fig. 2*b*. For both $\mathrm{T}^2_{1,f}$ (Figs. 9*a*–*f*) and $\mathrm{T}^2_{2,f}$ (Figs. 9*g*–*l*), the amplitude of the natural mode is higher than that of the forced mode, but the growth rates of both modes are close to zero (Figs. 9*c*,*i*), indicating that they are neither growing nor decaying with time. In addition to these two modes, there are also spectral peaks at linear combinations of f_1 and f_f (for $\mathrm{T}^2_{1,f}$) as well as f_2 and f_f (for $\mathrm{T}^2_{2,f}$). Although most of these combinatory modes are weak, a few of them can approach the magnitude of the forced mode, e.g. $f = 2f_1 - f_f$ for $\mathrm{T}^2_{1,f}$ (Fig. 9*b*) and $f = 3f_2 - f_f$ for $\mathrm{T}^2_{2,f}$ (Fig. 9*h*).

For $\mathrm{T}^2_{1,f}$ (Figs. 9*d*–*f*), the spatial distribution of the DMD modes is extracted at the three most dominant frequencies: (*d*) $\tilde{f} = 1.00$ for f_1, (*e*) $\tilde{f} = 1.08$ for

f_f, and (f) $\tilde{f} = 0.92$ for $2f_1 - f_f$. For $\mathrm{T}^2_{2,f}$ (Figs. 9j–l), the same procedure is performed: (j) $\tilde{f} = 0.74$ for f_2, (k) $\tilde{f} = 1.08$ for f_f, and (l) $\tilde{f} = 1.14$ for $3f_2 - f_f$. The DMD modes at the natural frequency (f_1 or f_2; Figs. 9d,j) share several common features with their counterparts from the periodic states of Figs. 7(g,h). These features include symmetric convective wavepackets and out-of-phase dynamics between the wavepackets on the inside of the flame front and those on the outside. However, the DMD modes at f_f exhibit a qualitatively different structure (Fig. 9e,k), with their support concentrated at the inner and outer edges of the unsteady flame front, in contrast to the more uniform distribution found in both the natural (f_1 or f_2) and forced (f_f) modes of the periodic states (Figs. 7g–i). The increased non-uniformity of the DMD modes at f_f (Fig. 9e,k) is thought to be due to interactions between the two frequencies of the quasiperiodic states, $\mathrm{T}^2_{1,f}$ and $\mathrm{T}^2_{2,f}$. In Fig. 9(e,k), the flame is perturbed at two incommensurate frequencies simultaneously: a natural mode (f_1 or f_2) and a forced mode (f_f). In Figs. 7(g–i), however, the flame is perturbed at just one frequency: a natural mode (f_1 or f_2). It is therefore sensible to expect the mode structure to be more intricate in the former case than in the latter case. The modes with the third highest spectral amplitude can be found at linear combinations of the natural and forcing frequencies (Fig. 9f,l). In these combinatory modes, the wavepackets exhibit a 'sandwich' pattern, with each wavepacket appearing as a superposition of multiple individual wavepackets from the forced (f_f) and natural (f_1 or f_2) modes.

In summary, this section has shown that, when compared with the periodic states of Sec. 3.2.1, the presence of two-frequency quasiperiodicity does not significantly alter the structure of the DMD modes at the natural frequency (f_1 or f_2). However, it does alter the structure of the DMD modes at the forcing frequency (f_f), by increasing the concentration of support at the inner and outer edges of the unsteady flame front.

3.2.3. Three-frequency quasiperiodic state: $\mathrm{T}^3_{1,2,f}$

Figure 10 is analogous to Figs. 7 and 9 but for the three-frequency quasiperiodic state identified in Figs. 2 and 4: $\mathrm{T}^3_{1,2,f}$. The amplitude spectrum (Fig. 10a) shows that the nonlinearly unstable natural mode (f_2) is stronger than the forced mode (f_f), which is itself stronger than the linearly unstable natural mode (f_1). This trend is consistent with the pressure spectra of Fig. 2b. All three of these modes are incommensurate with each other and have growth rates close to zero, indicating that they neither grow nor decay with time (Fig. 10b). Several of the linear combinations of the natural modes (f_1, f_2) and the forced mode (f_f) have higher amplitudes than the original natural mode (f_1) itself. This behavior was not observed in the periodic states (Fig. 7) or in the two-frequency quasiperiodic states (Fig. 9), demonstrating that robust three-frequency quasiperiodicity does not necessarily require all three constituent modes to be strong.

Figures 10(c–h) show the spatial distribution of the DMD modes at the six most dominant frequencies: (c) $\tilde{f} = 0.74$ for f_2, (d) $\tilde{f} = 1.00$ for f_1, (e) $\tilde{f} = 1.08$ for f_f, (f) $\tilde{f} = 0.34$ for $f_f - f_2$, (g) $\tilde{f} = 0.40$ for $2f_2 - f_f$, and (h) $\tilde{f} = 1.14$

for $3f_2 - f_f$. There are many similarities but also some key differences between these DMD modes ($\mathrm{T}^3_{1,2,f}$) and those from the periodic states (Fig. 7: $\mathrm{P1}_1$, $\mathrm{P1}_2$, $\mathrm{P1}_f$) and the two-frequency quasiperiodic states (Fig. 9: $\mathrm{T}^2_{1,f}$, $\mathrm{T}^2_{2,f}$). For example, at the nonlinearly unstable natural frequency of f_2, the flame structure for $\mathrm{T}^3_{1,2,f}$ (Fig. 10*c*) is remarkably similar to that for $\mathrm{P1}_2$ (Fig. 7*h*) and $\mathrm{T}^2_{2,f}$ (Fig. 9*j*), with broad convective wavepackets dominating the flame body. This is despite the present three-frequency quasiperiodic state having an extra degree of freedom over the periodic and two-frequency quasiperiodic states. However, at the original natural frequency of f_1, the wavepackets for $\mathrm{T}^3_{1,2,f}$ (Fig. 10*d*) are broader and less coherent than those for $\mathrm{P1}_1$ (Fig. 7*g*) and $\mathrm{T}^2_{1,f}$ (Fig. 9*d*), with a concentration of support located at the inner and outer edges of the flame. This shows that the flame response at f_1 is not particularly sensitive to the presence of a forced mode at f_f, but is exceedingly sensitive to the presence of a nonlinearly unstable natural mode at f_2. At the forcing frequency (f_f), the wavepackets for $\mathrm{T}^3_{1,2,f}$ (Fig. 10*e*) are broader and more uniformly distributed than those for $\mathrm{P1}_f$ (Fig. 7*i*), $\mathrm{T}^2_{1,f}$ (Fig. 9*e*) and $\mathrm{T}^2_{2,f}$ (Fig. 9*k*), with almost no evidence of the previously observed 'sandwich' structures (see Sec. 3.2.2).

For the combinatory modes at $f_f - f_2$ (Fig. 10*f*) and $2f_2 - f_f$ (Fig. 10*g*), we find long-wavelength modulations of the flame structure, which can be attributed to the lower frequencies of these modes: $\tilde{f} \sim 0.30$–0.40. For the mode at $3f_2 - f_f$ (Fig. 10*h*), which has a relatively high frequency of $\tilde{f} = 1.14$, the DMD structure qualitatively resembles that for $\mathrm{T}^2_{2,f}$ (Fig. 9*l*), with short-wavelength wavepackets and a similar 'sandwich' structure appearing in the flame body.

In summary, this section has shown that the flame structure at the nonlinearly unstable natural mode (f_2) is universally robust, with no variations across $\mathrm{P1}_2$, $\mathrm{T}^2_{2,f}$ and $\mathrm{T}^3_{1,2,f}$. The flame structure at the original natural mode (f_1) is robust only to the forced mode (f_f) but not to the f_2 mode, indicating the presence of asymmetric coupling in the flame response. This behavior may explain why the combustor dynamics converges to the f_2 mode, rather than the f_1 mode, as ϵ_f decreases from that required for $\mathrm{T}^3_{1,2,f}$ (Figs. 2 and 4).

4. Conclusions

In this experimental study, we have achieved two main research objectives (Sec. 1.3). First, we have demonstrated that it is readily possible to reduce the thermoacoustic amplitude of a self-excited combustion system through the strategic use of transient forcing, hysteresis and mode switching – thus avoiding the need to continuously supply energy to the control system (Sec. 3.1.6). This is achieved by exploiting the fact that most combustors have a multitude of natural thermoacoustic modes, some of which are linearly unstable but some are nonlinearly unstable [1, 46, 47]. By applying open-loop acoustic forcing at an off-resonance frequency and at an amplitude higher than that required for synchronization, we find that the combustor can switch to one of the nonlinearly unstable natural modes (f_2) and remain there, even after the forcing is removed. Dynamic mode decomposition of high-speed chemiluminescence videos shows that the flame structure at f_2 is more robust than that at the original natural mode (f_1), which could explain why the combustor dynamics converges to the f_2 mode, rather than the f_1 mode, when the forcing is removed (Sec. 3.2). Mode switching is caused by a change in the coupling process between unsteady combustion and acoustics. Its existence indicates that the combustor has multiple stable states, some of which can only be reached via the application and subsequent removal of strong external forcing. For this combustor, the final unforced state ($\mathrm{P1}_2$) has a thermoacoustic amplitude of just half that of the initial unforced state ($\mathrm{P1}_1$), even though the Rayleigh index of the former is higher than that of the latter (Fig. 4). Although this 50% reduction in thermoacoustic amplitude is not as large as the 95% reduction achieved with asynchronous quenching at the onset of synchronization ($\mathrm{P1}_f$), it is achieved without the use of continuous forcing. This is a distinct advantage over existing control strategies as it allows the complexity and power requirements of the control system to be reduced. With further development and testing, particularly on more realistic combustors featuring turbulent swirling flames, the proposed control strategy could pave the way for a new class of open-loop control techniques based on transient forcing, rather than continuous forcing. However, it should be noted that if stochastic forcing from turbulence is sufficiently strong, then that could itself trigger the nonlinearly unstable natural mode at f_2 without the need for external forcing, resulting in a two-frequency quasiperiodic state composed of natural modes f_1 and f_2. The forced synchronization of such a quasiperiodic state is the subject of active research [63].

Second, we have shown that a self-excited combustion system can exhibit an elaborate range of synchronization dynamics when forced at very high amplitudes. When the forcing amplitude increases from zero, reaches a maximum above that required for synchronization and then decreases back to zero, the combustor passes through a complex sequence of nonlinear states (Fig. 2): unforced periodicity ($\mathrm{P1}_1$) $\rightarrow$ two-frequency quasiperiodicity ($\mathrm{T}^2_{1,f}$) $\rightarrow$ synchronized periodicity ($\mathrm{P1}_f$) $\rightarrow$ three-frequency quasiperiodicity ($\mathrm{T}^3_{1,2,f}$) $\rightarrow$ two-frequency quasiperiodicity ($\mathrm{T}^2_{2,f}$) $\rightarrow$ unforced periodicity ($\mathrm{P1}_2$). Two features are particularly noteworthy: (i) mode switching and hysteresis occur along the routes to and from synchronization, with $\mathrm{P1}_1$ showing a different natural frequency than $\mathrm{P1}_2$ owing to the excitation of a linearly stable but nonlinearly unstable natural mode at f_2 (Fig. 4); and (ii) once synchronized, the combustor does not necessarily remain synchronized, but can transition to a three-frequency quasiperiodic state ($\mathrm{T}^3_{1,2,f}$) dominated by three incommensurate modes: the original natural mode (f_1), the new natural mode (f_2), and the forced mode (f_f). To the best of our knowledge, this is the first experimental observation of mode switching, hysteresis and three-frequency quasiperiodicity in a periodically forced self-excited combustor.

With regard to directions for future work, although our findings are qualitatively reproducible across different operating and forcing conditions, they have only been demonstrated here on one specific combustor, as a proof-of-concept initiative. In the nonlinear dynamics literature, it is well recognized that many of the defining features of forced synchronization are universal across physically disparate systems, ranging from flashing fireflies to circadian rhythms to triode circuits [21, 22]. Further experiments on increasingly realistic combustors should reveal the extent to which our findings carry over into industrial systems.

This work was funded by the Research Grants Council of Hong Kong (Projects 16235716 and 26202815).

References

[1] B. Zinn, T. Lieuwen, Combustion instabilities: Basic concepts, in: T. Lieuwen, V. Yang (Eds.), Combustion Instabilities in Gas Turbine Engines: Operational Experience, Fundamental Mechanisms, and Modeling, Progress in Astronautics and Aeronautics, American Institute of Aeronautics and Astronautics, Reston, VA, USA, 2005, Ch. 1.

[2] S. Candel, Combustion dynamics and control: Progress and challenges, Proceedings of the Combustion Institute 29 (1) (2002) 1–28.

[3] J. W. S. B. Rayleigh, The Theory of Sound, Vol. 2, Macmillan, 1896.

[4] T. C. Lieuwen, Unsteady Combustor Physics, Cambridge University Press, 2012.

[5] T. Poinsot, Prediction and control of combustion instabilities in real engines, Proceedings of the Combustion Institute 36 (1) (2017) 1–28.

[6] A. Epstein, Aircraft engines' needs from combustion science and engineering, Combustion and Flame 159 (2012) 1791–1792.

[7] J. O'Connor, S. Hemchandra, T. Lieuwen, Combustion instabilities in lean premixed systems, in: Lean Combustion (Second Edition), Elsevier, 2016, pp. 231–259.

[8] T. Lieuwen, B. Zinn, The role of equivalence ratio oscillations in driving combustion instabilities in low NO_x gas turbines, Proceedings of the Combustion Institute 27 (2) (1998) 1809–1816.

[9] F. Marble, S. Candel, Acoustic disturbance from gas non-uniformities convected through a nozzle, Journal of Sound and Vibration 55 (2) (1977) 225–243.

[10] T. Poinsot, A. Trouve, D. Veynante, S. Candel, E. Esposito, Vortex-driven acoustically coupled combustion instabilities, Journal of Fluid Mechanics 177 (1987) 265–292.

[11] A. P. Dowling, A. S. Morgans, Feedback control of combustion oscillations, Annual Review of Fluid Mechanics 37 (2005) 151–182.

[12] E. Lubarsky, D. Shcherbik, A. Bibik, B. Zinn, Open loop control of severe combustion instabilities by fuel flow modulation at non resonant frequencies, in: 42nd AIAA Aerospace Sciences Meeting and Exhibit, 2004, p. 634.

[13] J. H. Uhm, S. Acharya, Low-bandwidth open-loop control of combustion instability, Combustion and Flame 142 (4) (2005) 348–363.

[14] T. Yi, D. A. Santavicca, Forced flame response of turbulent liquid-fueled lean-direct-injection combustion to fuel modulations, Journal of Propulsion and Power 25 (6) (2009) 1259–1271.

[15] C. O. Paschereit, E. Gutmark, W. Weisenstein, Control of thermoacoustic instabilities in a premixed combustor by fuel modulation, 37th AIAA Aerospace Sciences Meeting and Exhibit.

[16] G. A. Richards, M. Janus, E. H. Robey, Control of flame oscillations with equivalence ratio modulation, Journal of Propulsion and Power 15 (2) (1999) 232–240.

[17] M. A. Heckl, Active control of the noise from a Rijke tube, Journal of Sound and Vibration 124 (1) (1988) 117–133.

[18] B. Ćosić, B. C. Bobusch, J. P. Moeck, C. O. Paschereit, Open-loop control of combustion instabilities and the role of the flame response to two-frequency forcing, Journal of Engineering for Gas Turbines and Power 134 (6) (2012) 061502.

[19] Y. Huang, V. Yang, Dynamics and stability of lean-premixed swirl-stabilized combustion, Progress in Energy and Combustion Science 35 (4) (2009) 293–364.

[20] H. C. Mongia, T. J. Held, G. C. Hsiao, R. P. Pandalai, Challenges and progress in controlling dynamics in gas turbine combustors, Journal of Propulsion and Power 19 (5) (2003) 822–829.

[21] A. Balanov, N. Janson, D. Postnov, O. Sosnovtseva, Synchronization: from simple to complex, Springer Science & Business Media, 2008.

[22] A. Pikovsky, M. Rosenblum, J. Kurths, Synchronization: A universal concept in nonlinear sciences, Cambridge University Press, 2003.

[23] L. K. B. Li, M. P. Juniper, Lock-in and quasiperiodicity in a forced hydrodynamically self-excited jet, Journal of Fluid Mechanics 726 (2013) 624–655.

[24] L. K. B. Li, M. P. Juniper, Phase trapping and slipping in a forced hydrodynamically self-excited jet, Journal of Fluid Mechanics 735 (2013) R5.

[25] M. P. Juniper, L. K. B. Li, J. W. Nichols, Forcing of self-excited round jet diffusion flames, Proceedings of the Combustion Institute 32 (1) (2009) 1191–1198.

[26] L. K. B. Li, M. P. Juniper, Lock-in and quasiperiodicity in hydrodynamically self-excited flames: Experiments and modelling, Proceedings of the Combustion Institute 34 (1) (2013) 947–954.

[27] A. R. Karagozian, L. Cortelezzi, A. Soldati, Manipulation and control of jets in crossflow, Vol. 439, Springer, 2014.

[28] S. Baek, H. Sung, Quasi-periodicity in the wake of a rotationally oscillating cylinder, Journal of Fluid Mechanics 408 (2000) 275–300.

[29] K. Kashinath, L. K. B. Li, M. P. Juniper, Forced synchronization of periodic and aperiodic thermoacoustic oscillations: lock-in, bifurcations and open-loop control, Journal of Fluid Mechanics 838 (2018) 690–714.

[30] Y. Guan, V. Gupta, K. Kashinath, L. K. B. Li, Open-loop control of periodic thermoacoustic oscillations: Experiments and low-order modelling in a synchronization framework, Proceedings of the Combustion Institute.

[31] Y. Guan, M. Murugesan, L. K. B. Li, Strange nonchaotic and chaotic attractors in a self-excited thermoacoustic oscillator subjected to external periodic forcing, Chaos: An Interdisciplinary Journal of Nonlinear Science 28 (9) (2018) 093109.

[32] B. Bellows, A. Hreiz, T. Lieuwen, Nonlinear interactions between forced and self-excited acoustic oscillations in premixed combustor, Journal of Propulsion and Power 24 (3) (2008) 628–631.

[33] S. Balusamy, L. K. B. Li, Z. Han, M. P. Juniper, S. Hochgreb, Nonlinear dynamics of a self-excited thermoacoustic system subjected to acoustic forcing, Proceedings of the Combustion Institute 35 (3) (2015) 3229–3236.

[34] J. W. Bennewitz, R. A. Frederick Jr, J. T. Cranford, D. M. Lineberry, Combustion instability control through acoustic modulation at the inlet boundary, Journal of Propulsion and Power 31 (6) (2015) 1672–1688.

[35] T. Biwa, S. Tozuka, T. Yazaki, Amplitude death in coupled thermoacoustic oscillators, Physical Review Applied 3 (3) (2015) 034006.

[36] T. Biwa, Y. Sawada, H. Hyodo, S. Kato, Suppression of spontaneous gas oscillations by acoustic self-feedback, Physical Review Applied 6 (4) (2016) 044020.

[37] E. Dewan, Harmonic entrainment of van der Pol oscillations: Phaselocking and asynchronous quenching, IEEE Transactions on Automatic Control 17 (5) (1972) 655–663.

[38] N. Minorsky, Comments "On asynchronous quenching", IEEE Transactions on Automatic Control 12 (2) (1967) 225–227.

[39] K. Kashinath, I. C. Waugh, M. P. Juniper, Nonlinear self-excited thermoacoustic oscillations of a ducted premixed flame: bifurcations and routes to chaos, Journal of Fluid Mechanics 761 (2014) 399–430.

[40] L. Kabiraj, A. Saurabh, N. Karimi, A. Sailor, E. Mastorakos, A. P. Dowling, C. O. Paschereit, Chaos in an imperfectly premixed model combustor, Chaos: An Interdisciplinary Journal of Nonlinear Science 25 (2) (2015) 023101.

[41] N. Noiray, D. Durox, T. Schuller, S. Candel, A unified framework for nonlinear combustion instability analysis based on the flame describing function, Journal of Fluid Mechanics 615 (2008) 139–167.

[42] S. Hong, S. J. Shanbhogue, R. L. Speth, A. F. Ghoniem, On the phase between pressure and heat release fluctuations for propane/hydrogen flames and its role in mode transitions, Combustion and Flame 160 (12) (2013) 2827–2842.

[43] H. Zhao, G. Li, D. Zhao, Z. Zhang, D. Sun, W. Yang, S. Li, Z. Lu, Y. Zheng, Experimental study of equivalence ratio and fuel flow rate effects on nonlinear thermoacoustic instability in a swirl combustor, Applied Energy 208 (2017) 123–131.

[44] B. Ahn, J. Lee, S. Jung, K. T. Kim, Low-frequency combustion instabilities of an airblast swirl injector in a liquid-fuel combustor, Combustion and Flame 196 (2018) 424–438.

[45] J. P. Moeck, C. O. Paschereit, Nonlinear interactions of multiple linearly unstable thermoacoustic modes, International Journal of Spray and Combustion Dynamics 4 (1) (2012) 1–27.

[46] M. P. Juniper, Triggering in the horizontal Rijke tube: non-normality, transient growth and bypass transition, Journal of Fluid Mechanics 667 (2011) 272–308.

[47] K. T. Kim, S. Hochgreb, Measurements of triggering and transient growth in a model lean-premixed gas turbine combustor, Combustion and Flame 159 (3) (2012) 1215–1227.

[48] J. O. Keller, K. Saito, Measurements of the combusting flow in a pulse combustor, Combustion Science and Technology 53 (2-3) (1987) 137–163.

[49] H. Kantz, T. Schreiber, Nonlinear time series analysis, Vol. 7, Cambridge University Press, 2004.

[50] A. H. Nayfeh, D. T. Mook, Nonlinear Oscillations, John Wiley & Sons, 2008.

[51] P. J. Schmid, Dynamic mode decomposition of numerical and experimental data, Journal of Fluid Mechanics 656 (2010) 5–28.

[52] P. J. Schmid, L. K. B. Li, M. P. Juniper, O. Pust, Applications of the dynamic mode decomposition, Theoretical and Computational Fluid Dynamics 25 (1-4) (2011) 249–259.

[53] C. W. Rowley, S. T. Dawson, Model reduction for flow analysis and control, Annual Review of Fluid Mechanics 49 (2017) 387–417.

[54] G. Berkooz, P. Holmes, J. L. Lumley, The proper orthogonal decomposition in the analysis of turbulent flows, Annual Review of Fluid Mechanics 25 (1) (1993) 539–575.

[55] A.-M. Kypraiou, A. Dowling, E. Mastorakos, N. Karimi, Proper orthogonal decomposition analysis of a turbulent swirling self-excited premixed flame, in: 53rd AIAA Aerospace Sciences Meeting, 2015, p. 0425.

[56] S. Mariappan, R. I. Sujith, P. J. Schmid, Experimental investigation of non-normality of thermoacoustic interaction in an electrically heated Rijke tube, International Journal of Spray and Combustion Dynamics 7 (4) (2015) 315–352.

[57] J.-F. Bourgouin, D. Durox, J. P. Moeck, T. Schuller, S. Candel, Self-sustained instabilities in an annular combustor coupled by azimuthal and longitudinal acoustic modes, in: ASME Turbo Expo 2013: Turbine Technical Conference and Exposition, American Society of Mechanical Engineers, 2013, pp. V01BT04A007–V01BT04A007.

[58] K. Aoki, M. Shimura, S. Ogawa, N. Fukushima, Y. Naka, Y. Nada, M. Tanahashi, T. Miyauchi, Short-and long-term dynamic modes of turbulent swirling premixed flame in a cuboid combustor, Proceedings of the Combustion Institute 35 (3) (2015) 3209–3217.

[59] P. Palies, M. Ilak, R. Cheng, Transient and limit cycle combustion dynamics analysis of turbulent premixed swirling flames, Journal of Fluid Mechanics 830 (2017) 681–707.

[60] C. Huang, W. E. Anderson, M. E. Harvazinski, V. Sankaran, Analysis of self-excited combustion instabilities using decomposition techniques, AIAA Journal (2016) 2791–2807.

[61] N. Karimi, M. J. Brear, S.-H. Jin, J. P. Monty, Linear and non-linear forced response of a conical, ducted, laminar premixed flame, Combustion and Flame 156 (11) (2009) 2201–2212.

[62] F. Baillot, D. Durox, R. Prud'Homme, Experimental and theoretical study of a premixed vibrating flame, Combustion and Flame 88 (2) (1992) 149–152.

[63] N. V. Stankevich, J. Kurths, A. P. Kuznetsov, Forced synchronization of quasiperiodic oscillations, Communications in Nonlinear Science and Numerical Simulation 20 (1) (2015) 316–323.

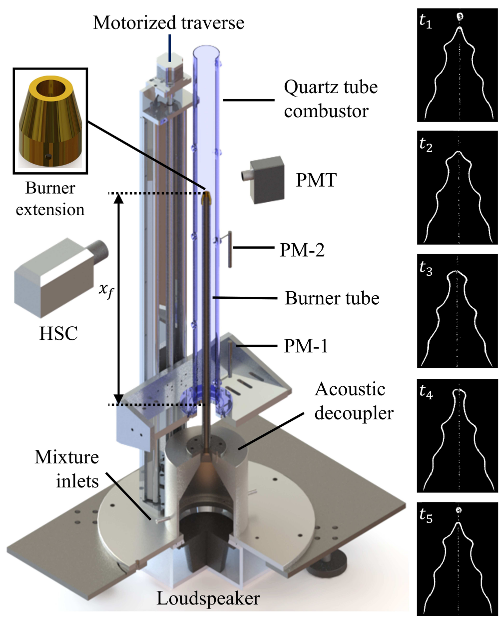

Figure 1: Illustration of the self-excited thermoacoustic system, which consists of a quartz tube combustor, a stainless steel burner, a copper burner extension, an acoustic decoupler with mixture inlets, a loudspeaker, and a motorized linear traverse for adjustment of the flame position ($x_f \equiv x/L$) within the combustor. The measurement diagnostics include two probe microphones (PM-1, PM-2), a hot-wire probe at the burner outlet (not shown), a high-speed camera (HSC), and a photomultiplier tube (PMT) fitted with a bandpass filter centered on 430 nm for CH* chemiluminescence detection. The insets along the right column are instantaneous inverse-Abel transformed images of the unsteady flame front for one complete cycle of the self-excited mode at $f_1 = 254$ Hz. These flame images were taken with the HSC and post-processed with an edge-detection algorithm. This figure is adapted from Ref. [30].

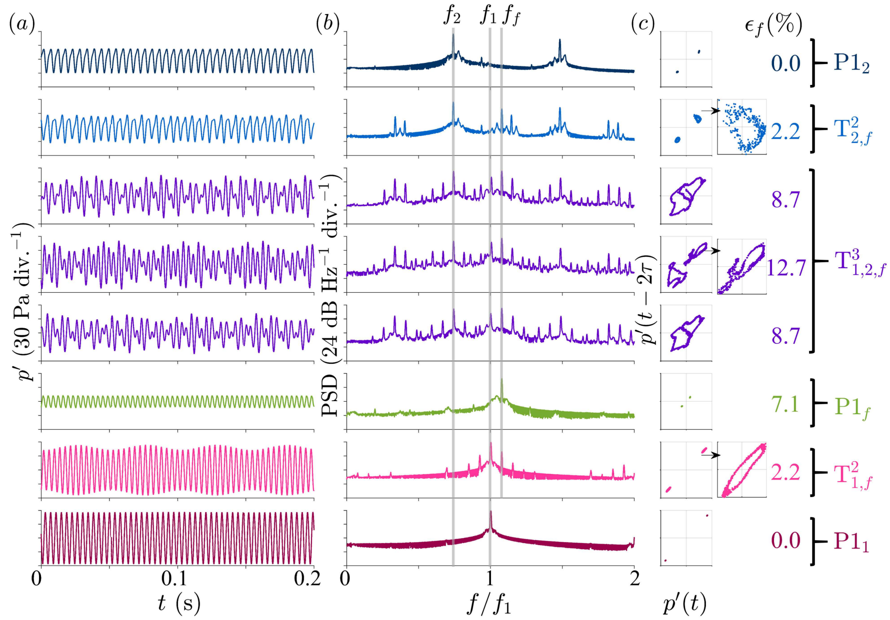

Figure 2: Forced synchronization of the self-excited thermoacoustic system at $f_f/f_1 \approx 1.08$. The (a) time trace, (b) PSD and (c) Poincaré map of the acoustic pressure in the combustor are shown for eight forcing amplitudes ($\epsilon_f \equiv u'/\bar{u}$). Period-1 attractors (limit cycles) are labelled as P1, two-frequency torus attractors are labelled as T^2, and three-frequency torus attractors are labelled as T^3. The frequency content of these attractors is indicated by the subscripts 1, 2 and f, which correspond respectively to the self-excited natural mode at f_1, the nonlinearly unstable natural mode at f_2, and the forced mode at f_f.

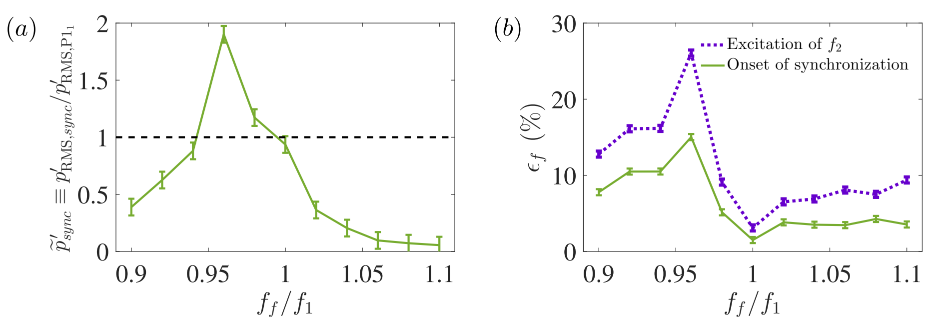

Figure 3: (a) Thermoacoustic amplitude at the onset of synchronization and (b) the minimum forcing amplitude required to produce synchronization and to excite the nonlinearly unstable natural mode (f_2), all plotted as a function of the forcing frequency (f_f/f_1).

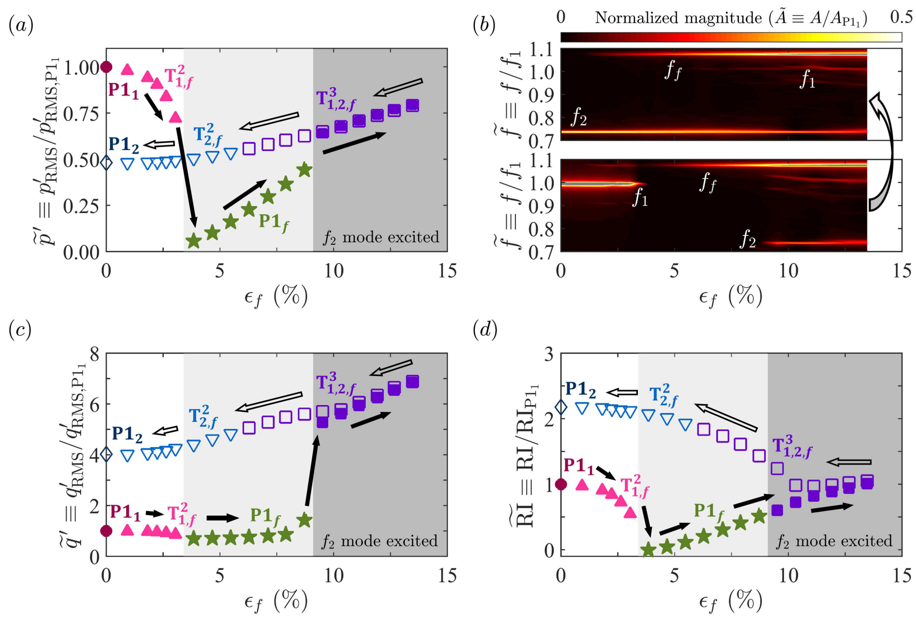

Figure 4: Control of self-excited thermoacoustic oscillations using transient forcing, hysteresis and mode switching at the conditions of Fig. 2 ($f_f/f_1 \approx 1.08$). Four indicators of the combustor are shown: (a) the RMS of p', (b) the PSD of p', (c) the RMS of q', and (d) the Rayleigh index. All four indicators are normalized by their respective values at the initial unforced state ($\mathrm{P1}_1$) and are plotted as a function of the forcing amplitude ($\epsilon_f \equiv u'/\bar{u}$). The filled markers are for the forward path (increasing ϵ_f), while the hollow markers are for the backward path (decreasing ϵ_f). In subfigure (b), the bottom frame is for the forward path (increasing ϵ_f), while the top frame is for the backward path (decreasing ϵ_f). In subfigures (a,c,d), the light gray region denotes potential synchronization, while the dark gray region denotes excitation of the nonlinearly unstable natural mode at f_2. At this forcing frequency ($f_f/f_1 \approx 1.08$), synchronization occurs via an inverse Neimark–Sacker bifurcation (i.e. a torus-death bifurcation), which causes phase trapping to occur just before the boundary between $\mathrm{T}^2_{1,f}$ and $\mathrm{P1}_f$.

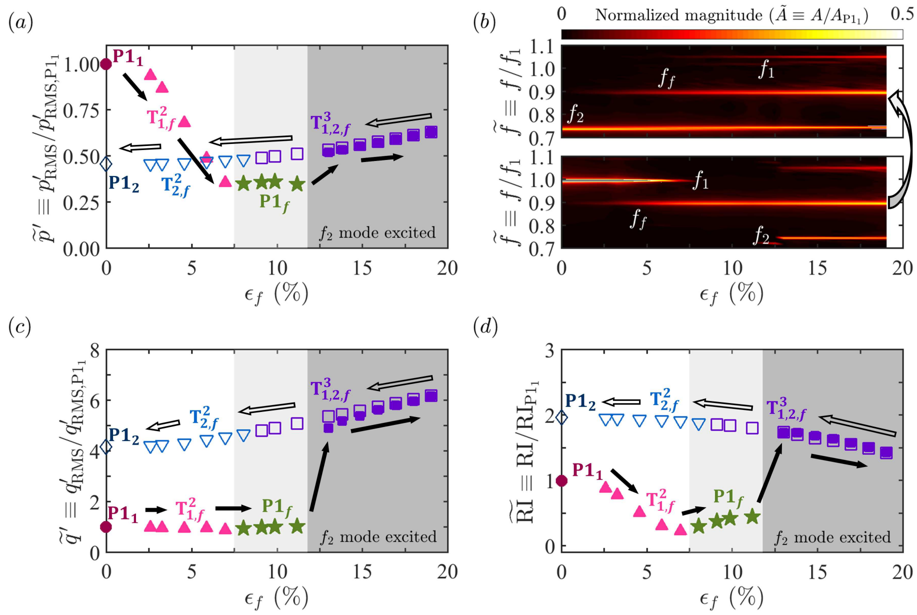

Figure 5: Demonstration of the robustness of the proposed strategy for controlling self-excited thermoacoustic oscillations. The quantities shown are the same as those in Fig. 4 but for $f_f/f_1 \approx 0.90$ instead of $f_f/f_1 \approx 1.08$. The filled markers are for the forward path (increasing ϵ_f), while the hollow markers are for the backward path (decreasing ϵ_f). In subfigure (*b*), the bottom frame is for the forward path (increasing ϵ_f), while the top frame is for the backward path (decreasing ϵ_f). In subfigures (*a*,*c*,*d*), the light gray region denotes potential synchronization, while the dark gray region denotes excitation of the nonlinearly unstable natural mode at f_2. At this forcing frequency ($f_f/f_1 \approx 0.90$), synchronization occurs via an inverse Neimark–Sacker bifurcation (i.e. a torus-death bifurcation), which causes phase trapping to occur just before the boundary between $\mathrm{T}^2_{1,f}$ and $\mathrm{P1}_f$.

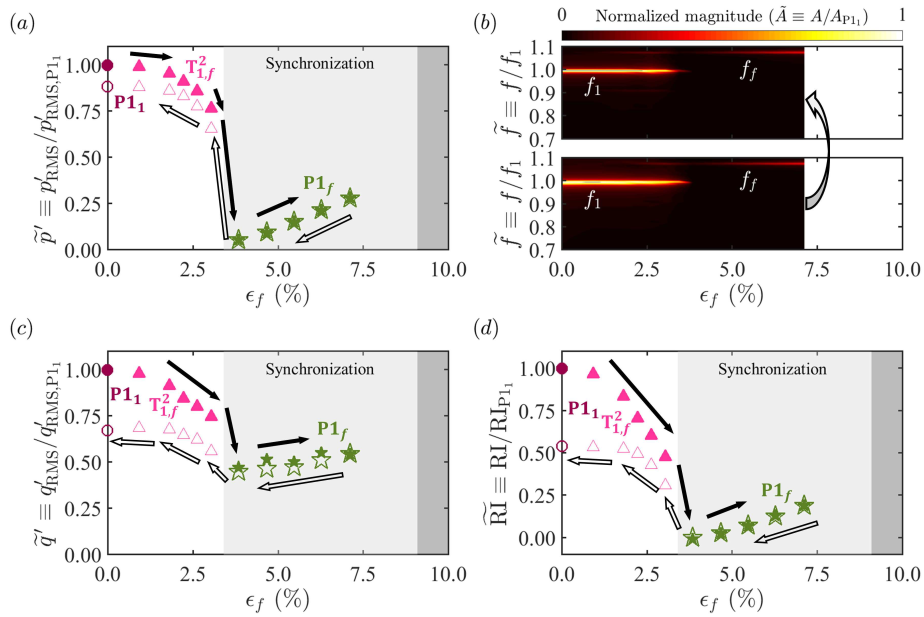

Figure 6: Example of a case without excitation of f_2 and thus without mode switching. The quantities shown are the same as those in Fig. 4 ($f_f/f_1 \approx 1.08$) but with ϵ_f increasing up to only the synchronized regime and then decreasing back to zero. The filled markers are for the forward path (increasing ϵ_f), while the hollow markers are for the backward path (decreasing ϵ_f). In subfigure (b), the bottom frame is for the forward path (increasing ϵ_f), while the top frame is for the backward path (decreasing ϵ_f). In subfigures (a,c,d), the light gray region denotes synchronization. At this forcing frequency ($f_f/f_1 \approx 1.08$), synchronization occurs via an inverse Neimark–Sacker bifurcation (i.e. a torus-death bifurcation), which causes phase trapping to occur just before the boundary between $\mathrm{T}^2_{1,f}$ and $\mathrm{P1}_f$.

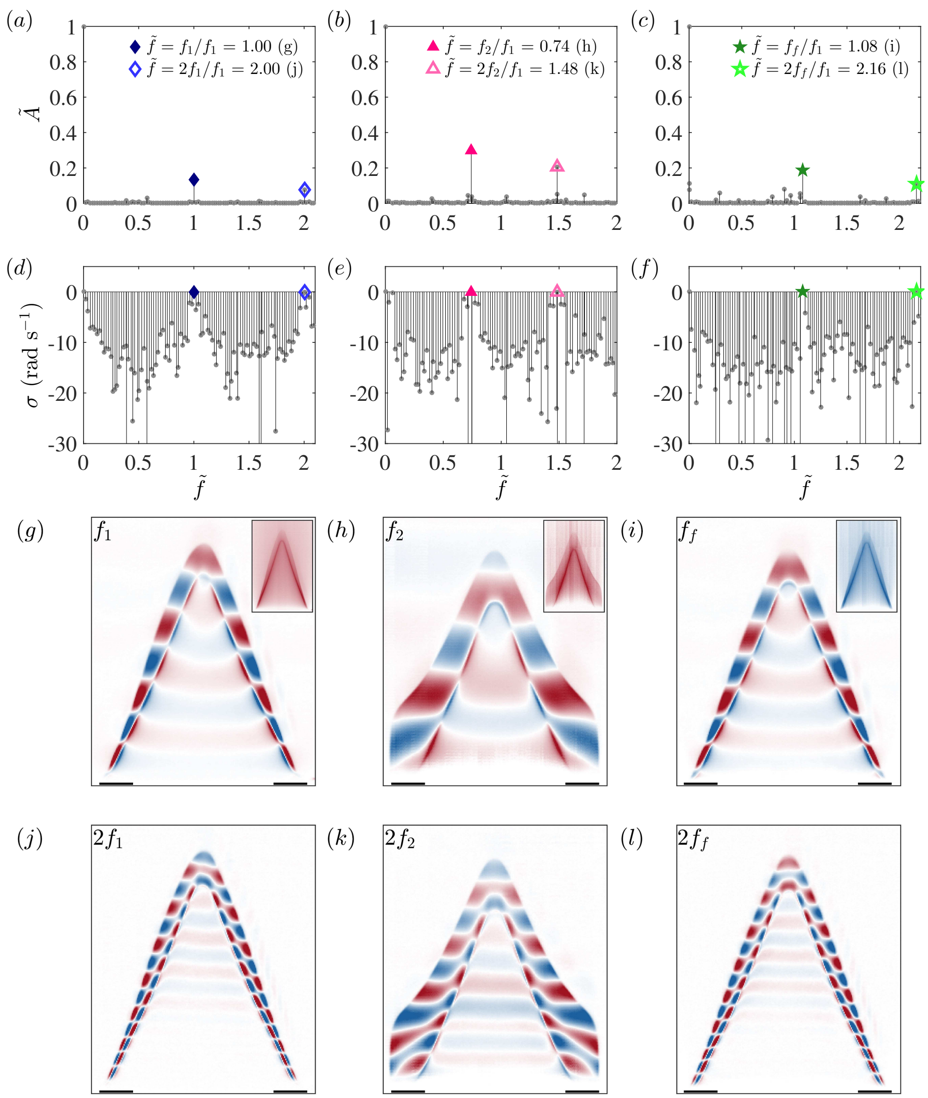

Figure 7: DMD of the flame chemiluminescence emission for the three different periodic states identified in Figs. 2 and 4, from left to right column: $P1_1$ (initial unforced state), $P1_2$ (final unforced state), and $P1_f$ (synchronized state). Shown are (*a*–*c*) the amplitude spectrum, (*d*–*f*) the growth rate spectrum, and (*g*–*l*) the dynamic modes (real part only), with the frequency indicated in the upper left corner. The modes shown in (*g*–*i*) are those with the highest spectral amplitude, while the modes shown in (*j*–*l*) are those with the second highest spectral amplitude. The insets in (*g*–*i*) are the modes at 0 Hz. The walls of the burner outlet extension (12 mm inner diameter) are shown at the bottom of (*g*–*l*).

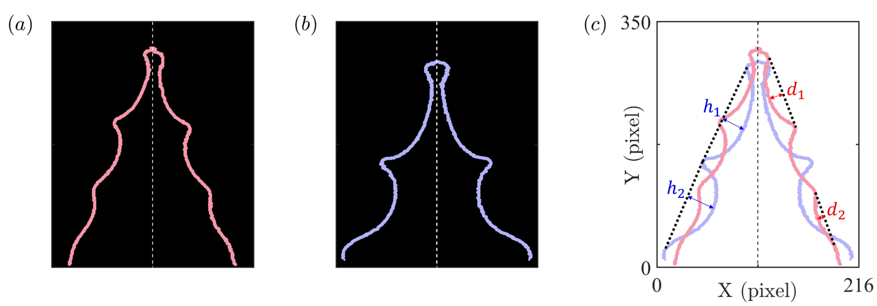

Figure 8: Comparison of the instantaneous flame fronts between two unforced periodic states: (a) P1_1, (b) P1_2, and (c) P1_1 and P1_2 overlaid on top of each other.

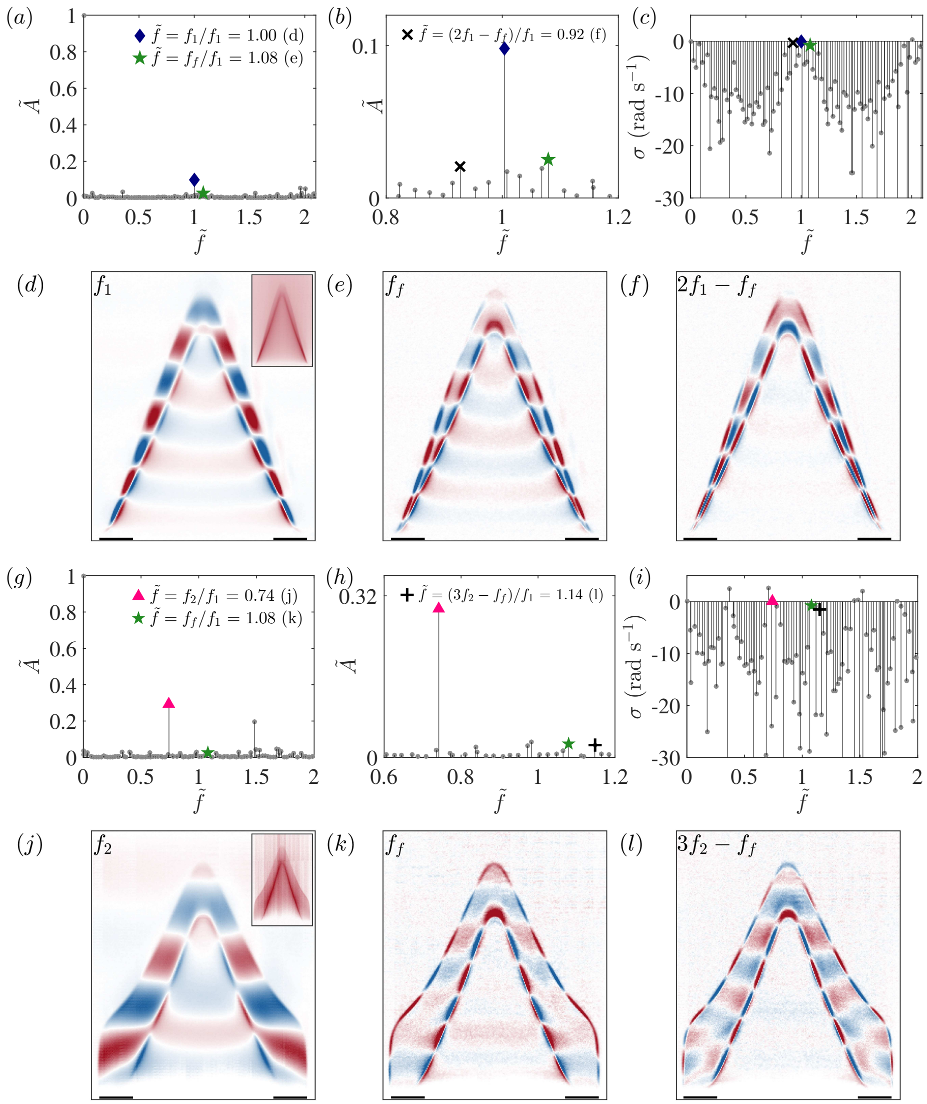

Figure 9: DMD of the flame chemiluminescence emission for the two different two-frequency quasiperiodic states identified in Figs. 2 and 4: (*a*–*f*) $\mathrm{T}^2_{1,f}$ and (*g*–*l*) $\mathrm{T}^2_{2,f}$. Shown are (*a*,*g*) the amplitude spectrum, (*b*,*h*) its magnified view, (*c*,*i*) the growth rate spectrum, and (*d*–*f*,*j*–*l*) the dynamic modes (real part only), with the frequency indicated in the upper left corner. For $\mathrm{T}^2_{1,f}$, the modes are extracted at (*d*) f_1, (*e*) f_f and (*f*) $2f_1 - f_f$. For $\mathrm{T}^2_{2,f}$, the modes are extracted at (*j*) f_2, (*k*) f_f and (*l*) $3f_2 - f_f$. The insets in (*d*,*j*) are the modes at 0 Hz. The walls of the burner outlet extension (12 mm inner diameter) are shown at the bottom of (*d*–*f*) and (*j*–*l*).

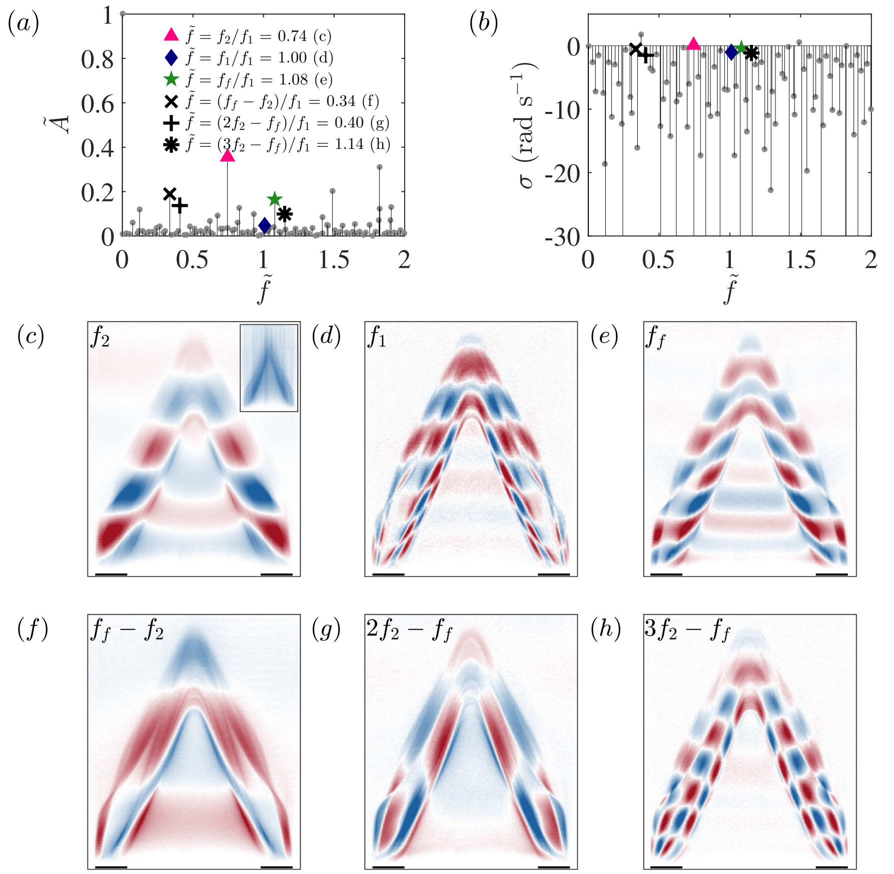

Figure 10: DMD of the flame chemiluminescence emission for the three-frequency quasiperiodic state identified in Figs. 2 and 4: $\mathrm{T}^3_{1,2,f}$. Shown are (*a*) the amplitude spectrum, (*b*) the growth rate spectrum, and (*c*–*h*) the dynamic modes (real part only), with the frequency indicated in the upper left corner. The modes are extracted at (*c*) f_2, (*d*) f_1, (*e*) f_f, (*f*) $f_f - f_2$, (*g*) $2f_2 - f_f$, and (*h*) $3f_2 - f_f$. The inset in (*c*) is the mode at 0 Hz. The walls of the burner outlet extension (12 mm inner diameter) are shown at the bottom of (*c*–*h*).

Figure 1
Click here to download Figure: fig1.eps

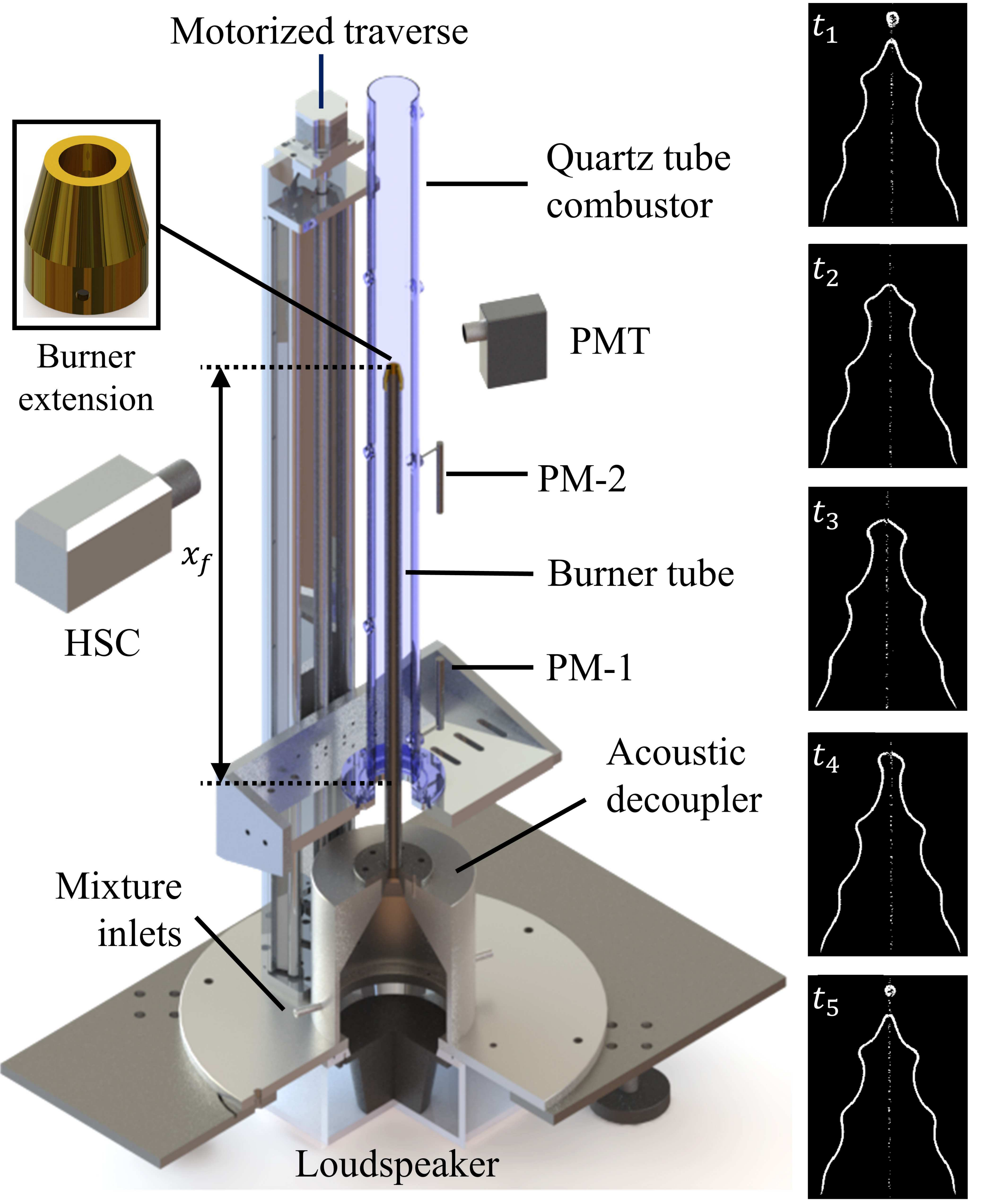

Figure 2
Click here to download Figure: fig2.eps

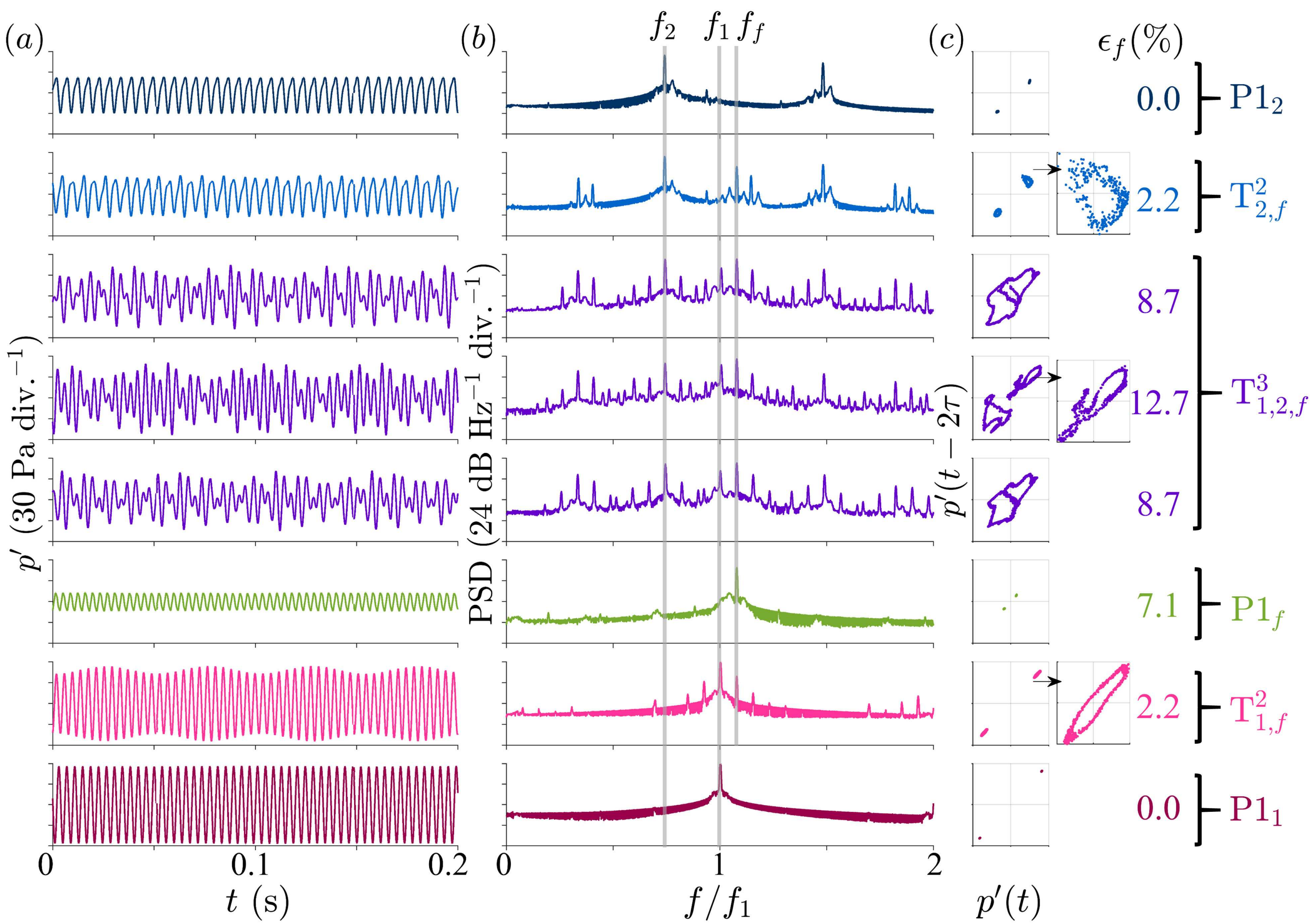

Figure 3
Click here to download Figure: fig3.eps

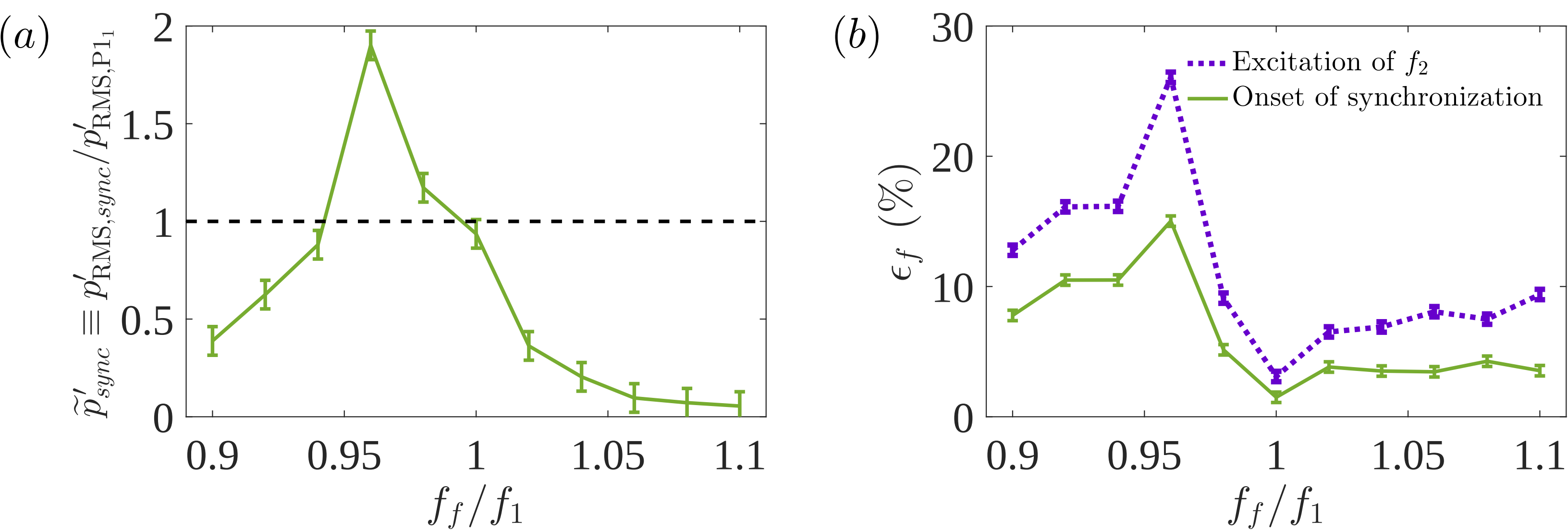

Figure 4
Click here to download Figure: fig4.eps

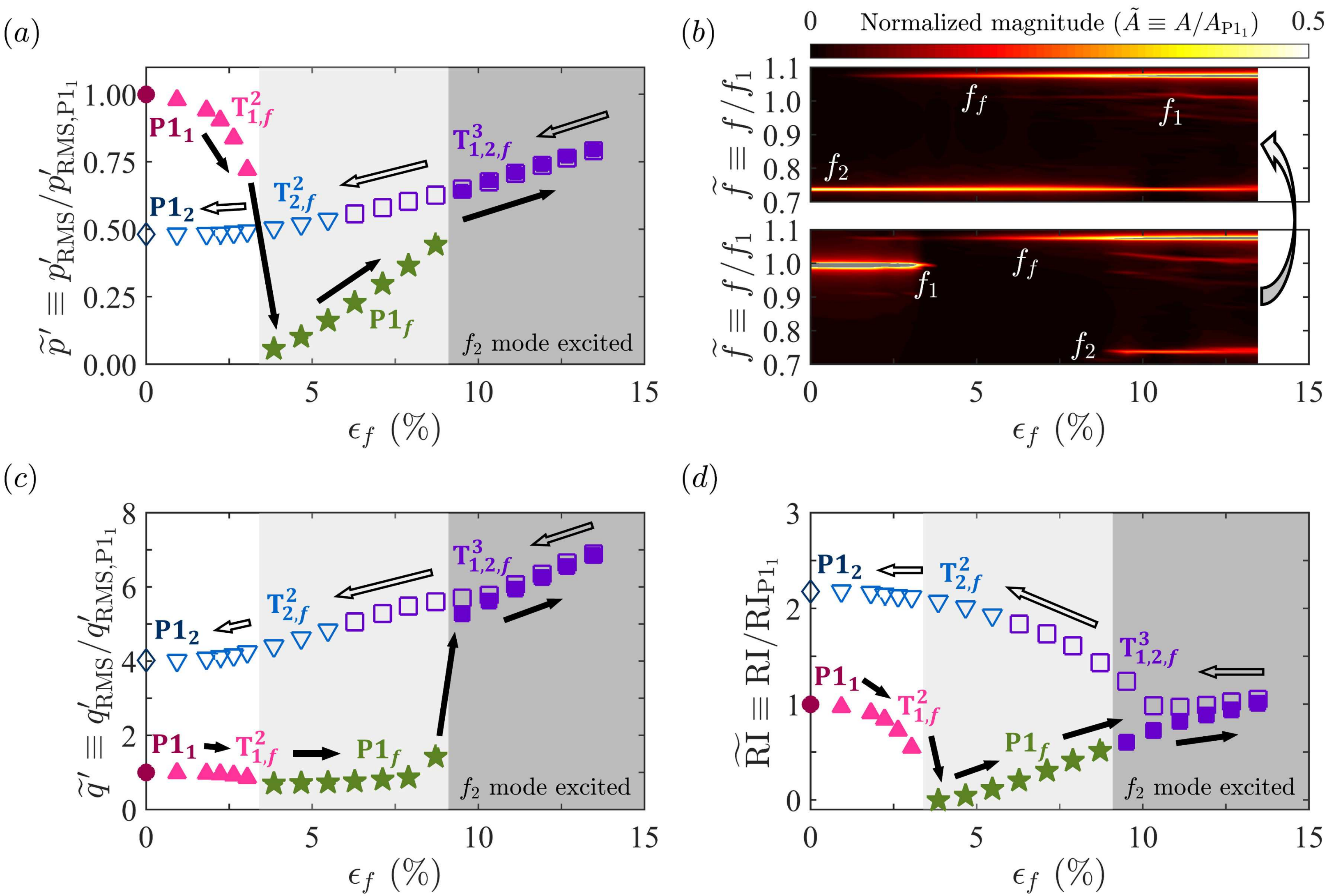

Figure 5

Click here to download Figure: fig5.eps

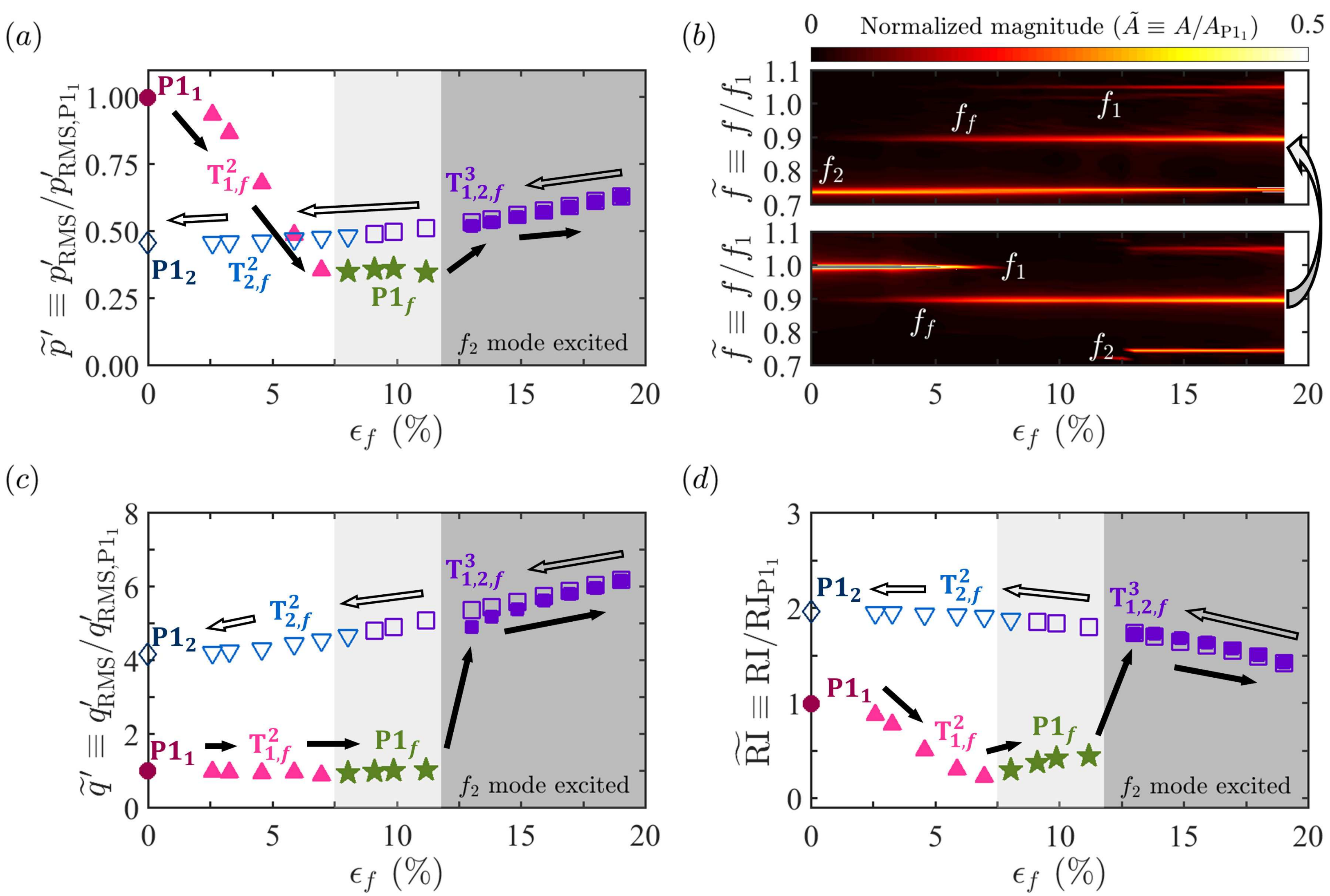

Figure 6

Click here to download Figure: fig6.eps

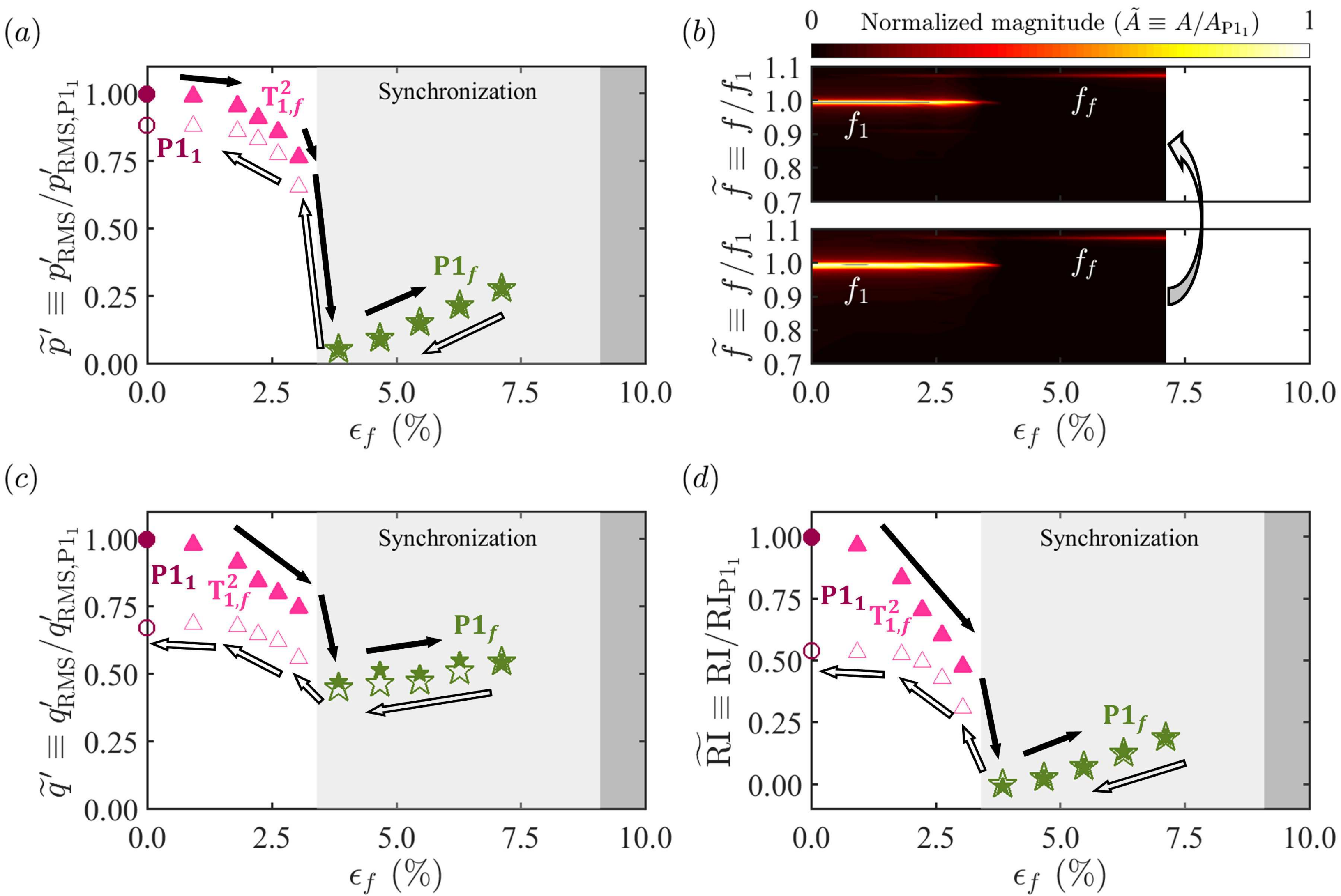

Figure 7abcdef

Click here to download Figure: fig7abcdef.eps

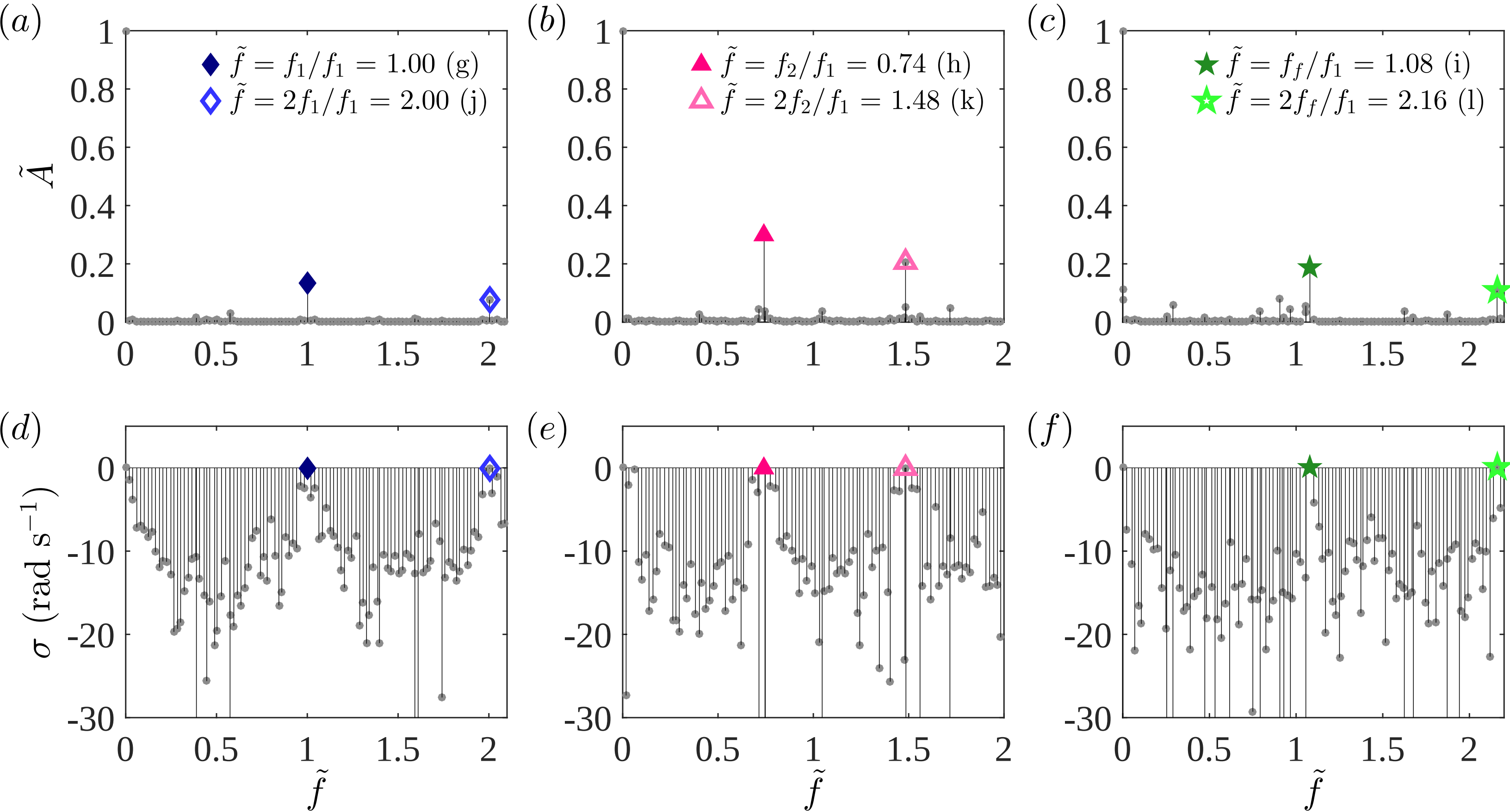

Figure 7ghi

Click here to download Figure: fig7ghi.eps

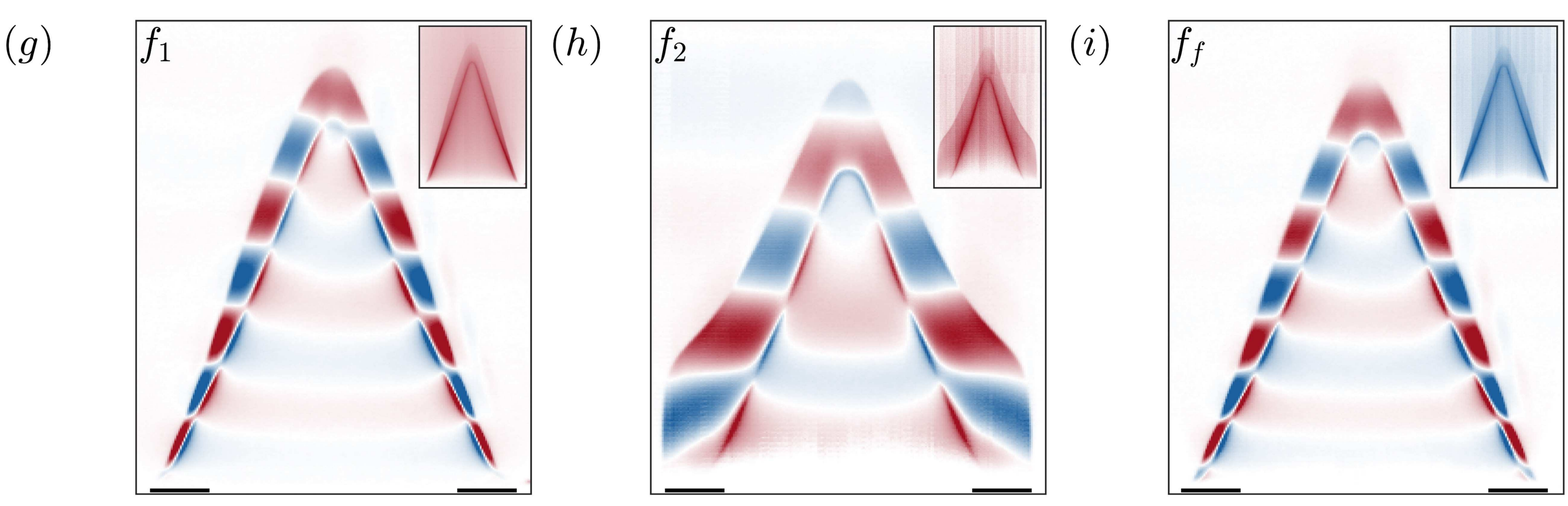

Figure 7jkl
Click here to download Figure: fig7jkl.eps

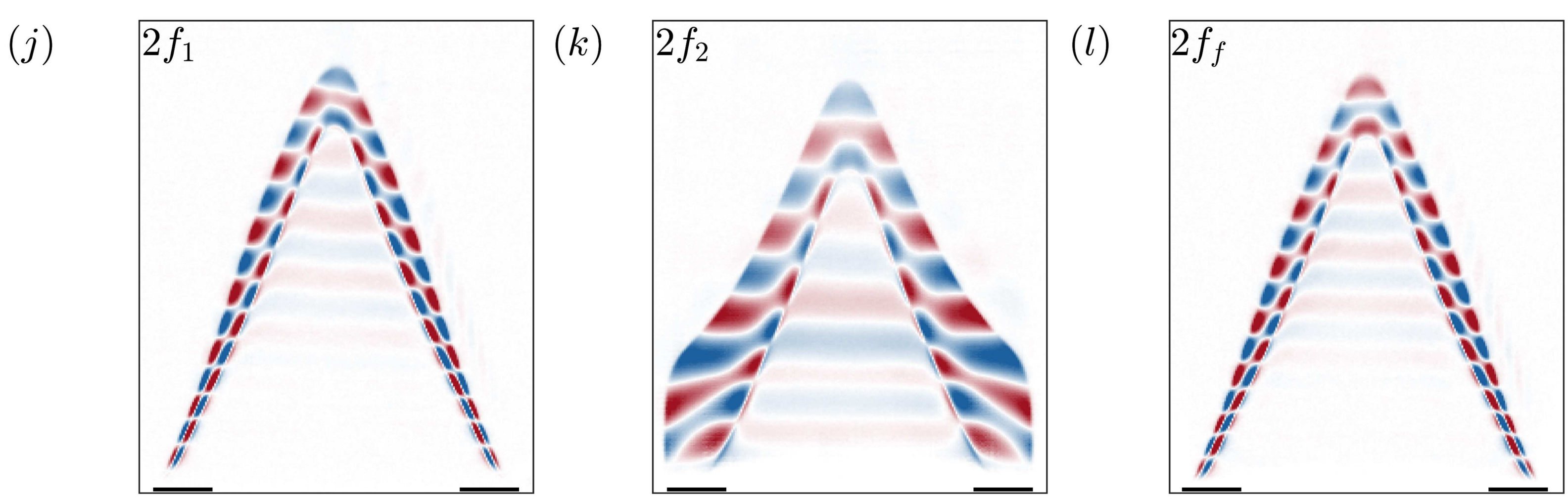

Figure 8
Click here to download Figure: fig8.eps

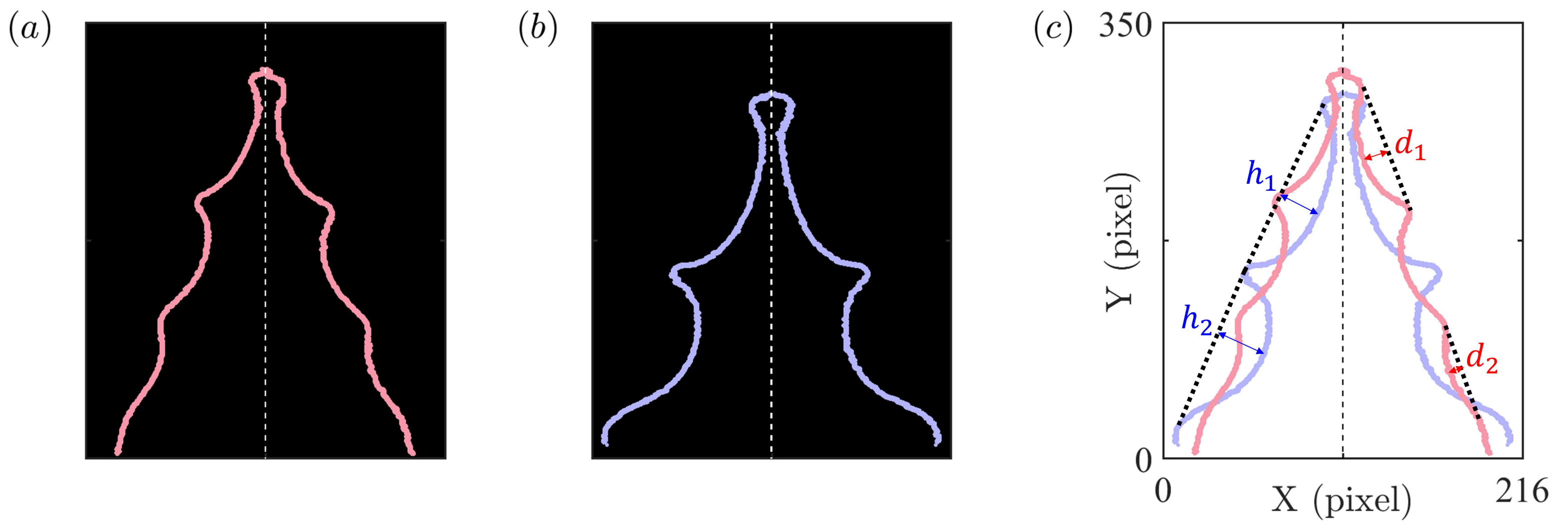

Figure 9abc

Click here to download Figure: fig9abc.eps

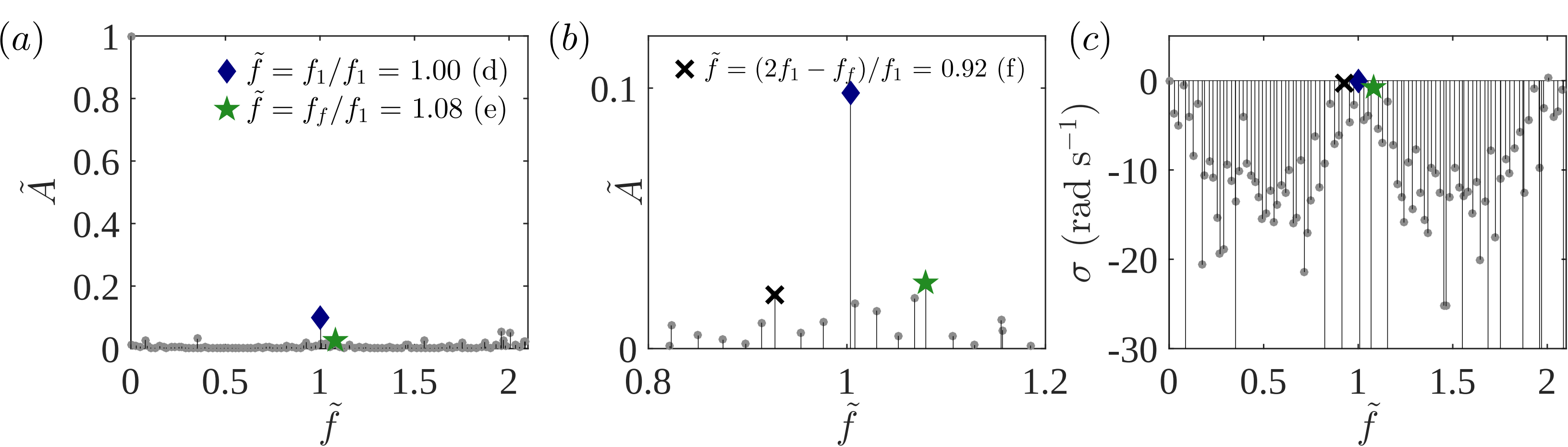

Figure 9def

Click here to download Figure: fig9def.eps

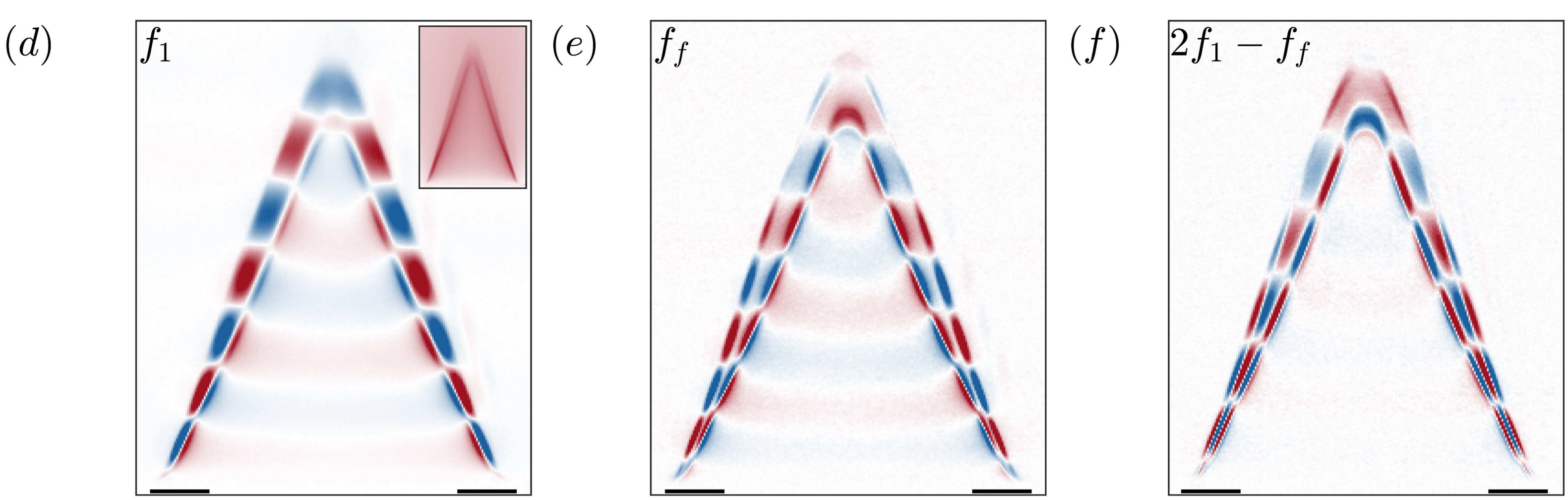

Figure 9ghi
Click here to download Figure: fig9ghi.eps

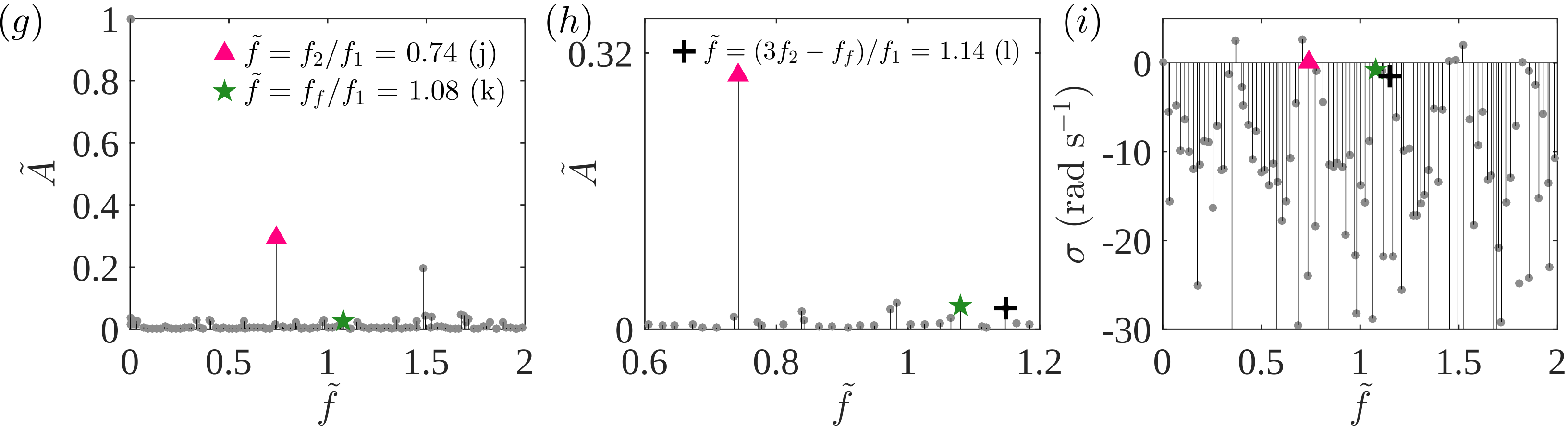

Figure 9jkl
Click here to download Figure: fig9jkl.eps

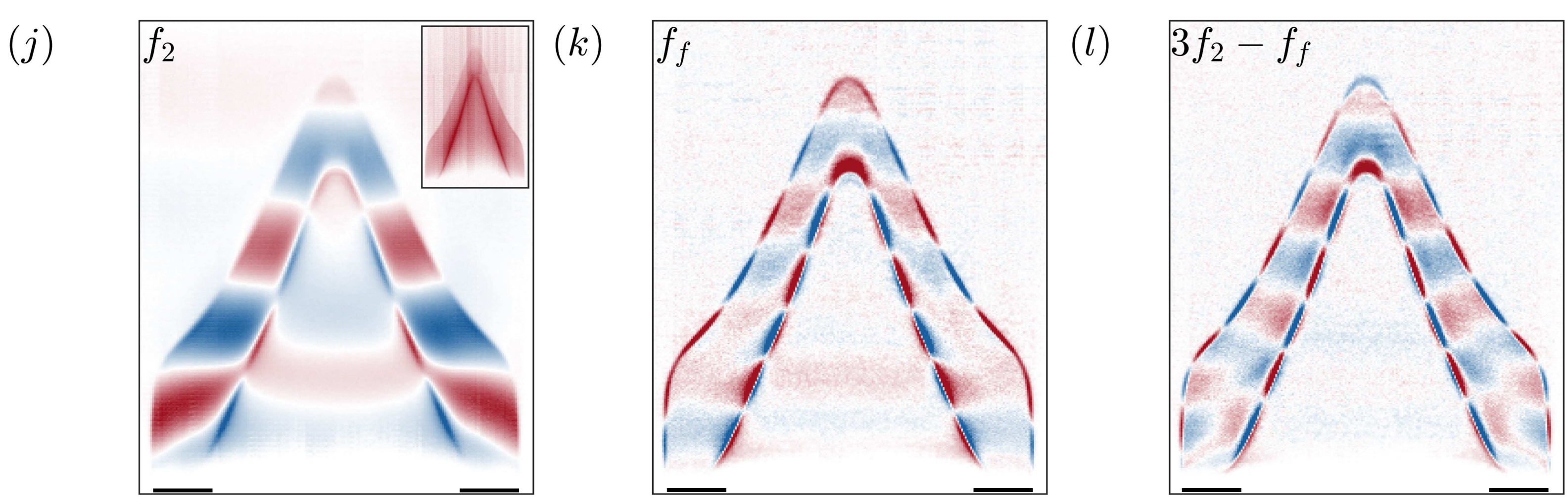

Figure 10ab
Click here to download Figure: fig10ab.eps

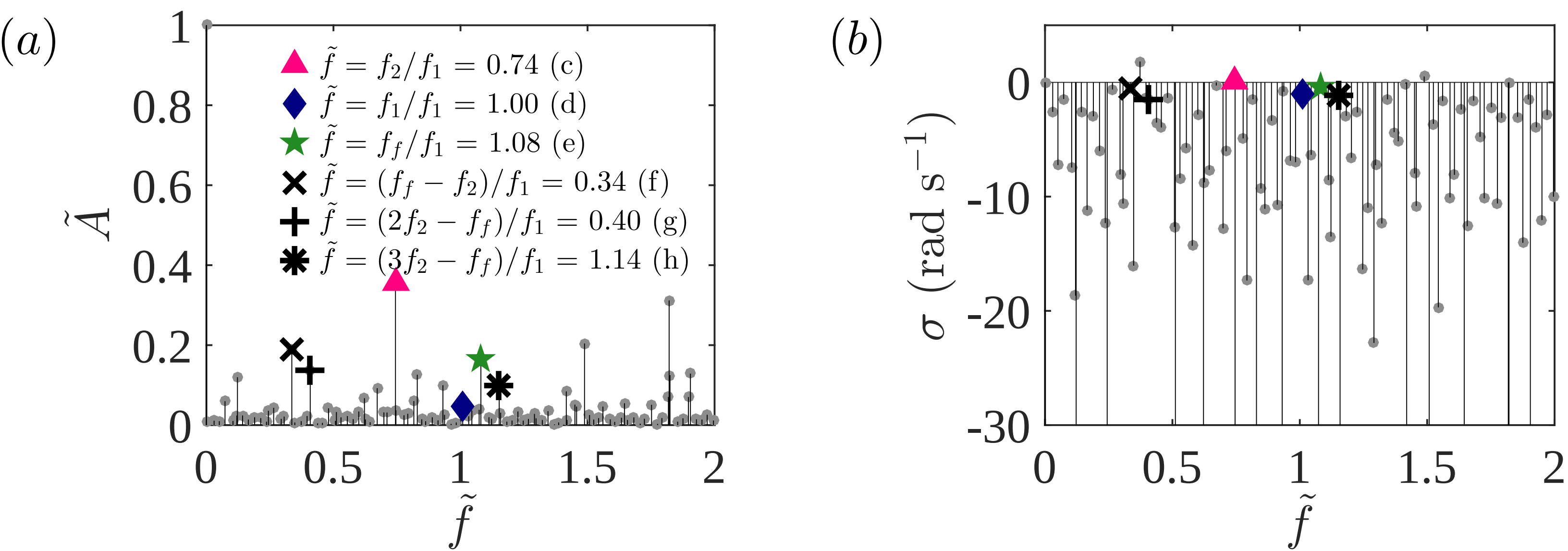

Figure 10cde

Click here to download Figure: fig10cde.eps

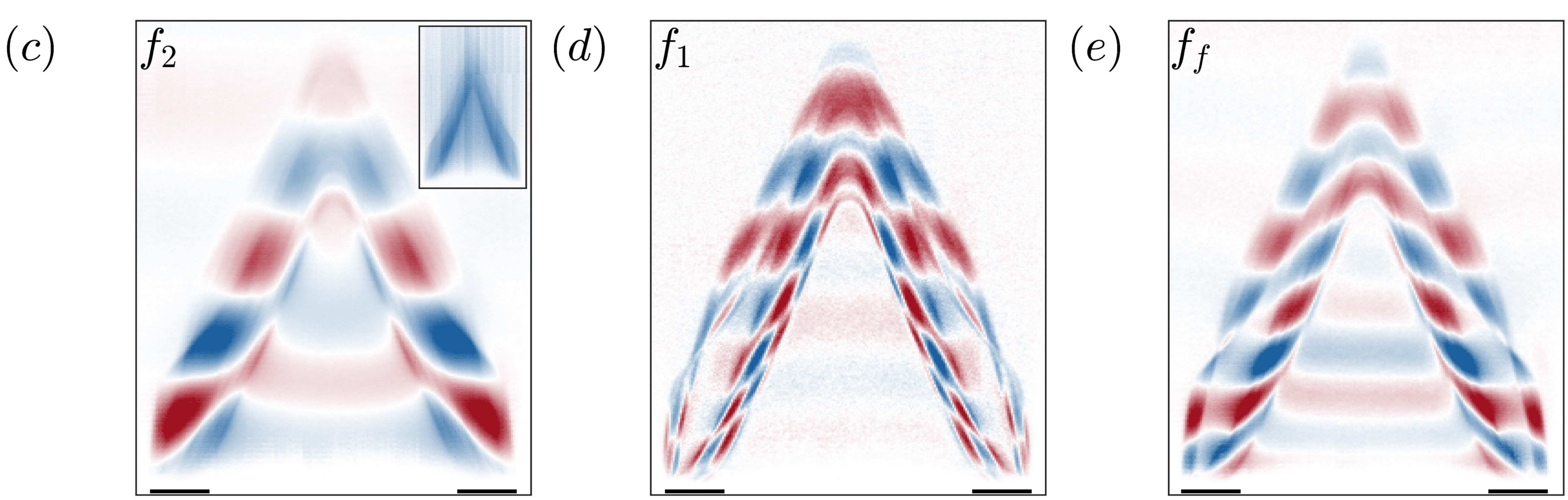

Figure 10fgh

Click here to download Figure: fig10fgh.eps

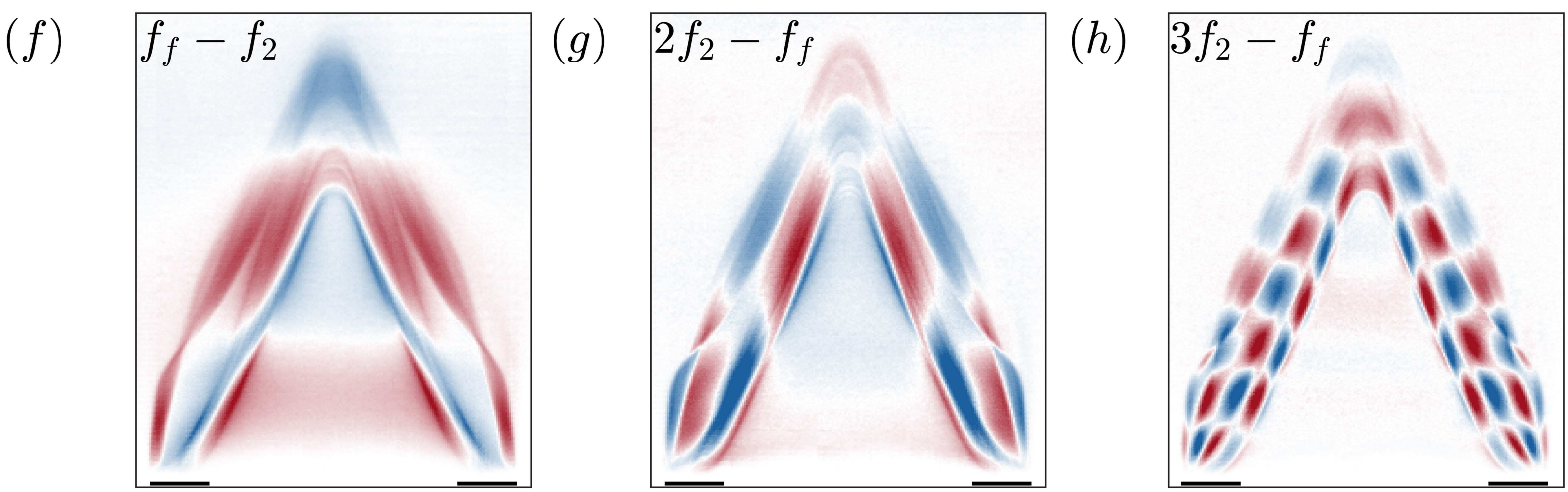

Bibliography

Click here to download LaTeX Source Files: main-bibfile.bib